UNIVERSITY OF CAMBRIDGE
Department of Engineering

Visualisation of Floatation of Tunnels Following Earthquake-Induced Liquefaction

Author Name: Ewan Taylor (PEM)
Supervisor: Prof. S.P.G. Madabhushi

Date: 29th May 2019

I hereby declare that, except where specifically indicated, the work submitted herein is my own original work.

Signed: ______________________ Date: 29/05/19

ENGINEERING TRIPOS PART IIB PROJECT

VISUALISATION OF FLOATATION OF TUNNELS FOLLOWING EARTHQUAKE-INDUCED LIQUEFACTION

TECHNICAL ABSTRACT

Ewan Taylor (PEM) Supervisor: Prof. SPG Madabhushi 29th May 2019

Liquefaction is a phenomenon where soils lose their strength and stiffness during earthquake loading. The loss in strength means lightweight buried structures such as pipelines and tunnels can uplift, as their buoyancy is no longer restrained by the overlying soil. This can damage the buried structure and nearby surface structures, with potential for human and economic cost. Buried structures are becoming increasingly important for the transportation of services, utilities and people in congested urban areas. Therefore research in to different remediation schemes is important to guide cost-effective and safe design of tunnels to protect them from uplift failure.

The aim of this project was to investigate the use of simple ground improvement schemes as a remediation technique for this problem. Small-scale 1-g shaking table tests were performed with different geometries of compacted, coarse-granular fill used to replace areas of the liquefiable layer around the model tunnel. Four remediation layouts were tested including: a reference test with no remediation, a block of granular fill placed beneath the tunnel invert, a narrow block of granular fill placed above the tunnel crown, and a wide block of granular fill placed above the tunnel crown. For the test with granular fill beneath the tunnel, the foundation soil was also denser than for other tests. The liquefiable layer was formed from loose Hostun sand, and the granular fill blocks from compacted Fraction A sand. All tests were saturated with water. Each test was filmed through a window in the model container and Particle Image Velocimetry (PIV) used to visualise the uplift mechanisms.

Ground improvement performed beneath the tunnel was most successful at reducing uplift, with a final uplift displacement of 25 mm. Ground improvement performed above the tunnel showed virtually no benefit compared to the reference test, with all achieving uplift displacements of over 65 mm. These results have been linked to how the ground improvement influenced the soil deformation mechanisms during the uplift.

PIV analysis of the reference test showed that whilst the tunnel uplifted, the soil deformed in a

large circular mechanism, with liquefied soil flowing from the crown, down the sides of the tunnel, and up towards the invert. A near identical uplift mechanism was seen for both tests with ground improvement above the tunnel. Meanwhile, with ground improvement beneath the tunnel, the uplift mechanism was limited to small flows of soil down the sides of the tunnel towards the invert. By restricting the flow of liquefied soil around the tunnel, mobilisation of the large circular uplift mechanism was prevented and so the ground improvement beneath the tunnel was successful at limiting uplift.

PIV was also used to analyse the sub-cyclic uplift mechanisms. For all tests, two distinct, asymmetric soil deformation mechanisms were seen, each lasting for half a cycle. It was observed that the tunnel ratcheted up through the liquefied soil via the sub-cyclic mechanisms, leading to a double-input frequency cyclic component to the uplift. The asymmetric nature of the sub-cyclic mechanisms also resulted in rocking of the tunnel at the input frequency as it uplifted.

Excess Pore Pressure (EPP) was measured at the tunnel invert and in the far-field. Invert EPP was consistently lower than far-field EPP, due to dynamic soil-structure interaction effects. When ground improvement was performed beneath the tunnel, the EPP at the invert was lower than for all other tests. This reduced the force on the invert driving the tunnel upwards, leading to the lower uplift seen for this test. Meanwhile for the other tests, equilibrium analysis of the force components acting on the tunnel showed that, even if ground improvement above the tunnel was able to maintain full shear strength in the backfill, the generation of EPP at the invert still resulted in a net upwards force. The subsequent inability of the overlying ground remediation to inhibit the large circular uplift mechanism resulted in large uplift in these tests. This suggests that, for shallow tunnels at this scale, disrupting the flow of liquefied soil around the tunnel and alleviating EPP acting on the invert is more important than retaining shear strength on planes above the tunnel when attempting to limit uplift.

Contents

1 Introduction

1.1 Overview

This MEng project investigated the design of remediation schemes to prevent the uplift of tunnels following earthquake-induced liquefaction. Four 1-g shaking table tests were conducted, each containing a different geometry of coarse-grained granular fill inclusion, to attempt to reduce tunnel uplift upon shaking. This report contains a review of literature relevant to this area, details the experimental methodology, and reports and discusses key results.

1.2 Motivation

Liquefaction is a phenomenon where soils lose their strength and stiffness during earthquake loading. This means that lightweight buried structures such as pipelines and tunnels can uplift, as their buoyancy is no longer restrained by the overlying soil. In an increasingly congested urbanised world, buried lifelines are vital for the transportation of services, utilities, and people. Uplift during an earthquake can cause damage to the buried structure itself and nearby surface structures, with the potential for economic and human cost. Research into the mechanisms of tunnel uplift and the effectiveness of different remediation measures is important to inform the design of structures so they remain serviceable during and after earthquakes, avoid damage to the surroundings, and prevent loss of life.

The detrimental effects of uplift on small-scale buried structures were witnessed following the 2011 Tohoku Pacific earthquake in Japan. In Urayasu City near Tokyo, 28.6 km of sewer pipelines were damaged (Chian et al., 2014), in some cases by uplifting as shown in figure 1. Uniform large-displacement uplift of a structure can render it unserviceable, especially if the ground surface is ruptured. Meanwhile Tokimatsu et al. (2013) report that near Kamisu city, buried utility conduits serving the Wanigawa water purification plant uplifted by 40 cm relative to the piled building, as seen in figure 2. The resulting shear failure of the conduit severed electrical wiring into the plant, preventing its operation. The settlement trough created by an uplifting buried structure can also cause damage to surface structures by imposing differential settlements. A further hazard is the possibility of differential uplift and settlement along the length of a buried structure. Imposed bending strains along the structure can cause bending failure, which can open up joints causing flooding. Pease and O'Rourke (1997) identified this was of concern where structures cross boundaries between liquefiable and non-liquefiable deposits.

Figure 1: Uplift of underground utility in Chiba (Tokyo metro) area (Structural Engineers Association of Washington, 2011)

Figure 2: Uplift of utility conduit at water purification plant in Kamisu city, Ibaraki Prefecture (Tokimatsu et al., 2013)

Whilst there are currently no reports of uplift for large transportation tunnels, the potential risk has been identified in several cases. A seismic retrofit program for the George Massey tunnel near Vancouver, Canada, between 2000 and 2006 included in-situ densification and installation of gravel drains in the surrounding soils to reduce uplift risk, and strengthening of the tunnel lining (Taylor et al., 2005). For the Marmaray tunnel in Istanbul, Turkey, the risk of uplift was mitigated through a compaction grouting scheme and replacement of liquefiable back fill (Yamamoto et al., 2014). For the Bay Area Rapid Transit (BART) Transbay Tubes in San Francisco, California, USA, numerical analyses (Chang et al., 2008; Chou et al., 2010) and centrifuge model tests (Kutter et al., 2008; Chou et al., 2011) were conducted to assess liquefaction and uplift potential. However, in this case, it was deemed that the predicted uplift displacement was not large enough to warrant an expensive remediation programme.

In summary, remediation schemes, whilst expensive, are necessary when the risk of severe damage from large uplift is identified. Further research is needed in to different remediation schemes to guide cost-effective and safe tunnel design.

1.3 Aims and Scope

The aim of this project was to investigate the use of simple ground improvement schemes as a remediation technique for this problem; specifically, the use of compacted, coarse-grained granular fill inclusions to replace areas of the liquefiable layer around the tunnel. Four small-scale model tests were conducted on a 1-g shaking table, using a transparent window box, and Particle Image Velocimetry (PIV) analysis was used to visualise soil deformations around the tunnel.

For each test, a different geometry of granular fill was placed around the semi-elliptical model tunnel. The geometry of the granular fill inclusion for each case was designed to limit uplift by targeting key aspects of the uplift mechanisms identified in literature (section 2), including: restoring shear strength on planes above the tunnel, increasing the unit weight of backfill to weigh down the tunnel, relieving excess pore pressure acting on the invert, and restricting the flow of liquefied soil around the tunnel.

The extremely non-linear properties of soil are heavily dependent on confining stresses. Field-scale soil characteristics can be accurately replicated at small-scale in geotechnical centrifuge testing, but not with 1-g testing, as the low confining stresses result in differing soil behaviour. The intention is therefore to provide a preliminary indication of the effect of the remediation measures on tunnel uplift. Results will be compared between the models, but will not be scaled to field conditions. Further investigation with geotechnical centrifuge and/or numerical modelling is required to obtain results that can be used to directly inform design.

2 Literature Review

2.1 Soil Liquefaction

Earthquake-induced liquefaction can occur in cohesionless soils which are loosely packed and are highly saturated. The cyclic loading of the earthquake causes liquefaction with a resulting drop in soil strength and stiffness. Seed and Idriss (1982) offer an explanation of the mechanism behind liquefaction. Ground accelerations during an earthquake cause cyclic shear waves to propagate rapidly through the soil. Loose sands tend to contract on shearing; the initially loose soil skeleton collapses into a denser structure as the soil grains try to rearrange into a state with lower gravitational potential energy. However, during an earthquake this tendency to contract happens on a quicker timescale than the pore water can flow out of the voids. This results in total stresses falling onto the pore water, leading to the generation of excess pore pressures (EPP), with a corresponding drop in effective stress between grains. As the effective stresses in the soil reduce, the soil skeleton will rebound which will act to alleviate the contraction originally causing the increase in EPP. Therefore the magnitude of EPP reached in the soil will depend on interaction between the volume reduction due to imposed shearing and soil skeleton rebound (Martin et al., 1975). Soils are frictional materials, whose shear strength depends on the confining effective stress. If during an earthquake EPP builds up and the effective stress reduces, shear strength will reduce as a consequence.

A convenient way to assess the extent of liquefaction in soil is by the liquefaction ratio, defined:

$$r_u = \frac{\Delta u}{\sigma'_{vo}} \tag{1}$$

where r_u is the liquefaction ratio, Δu is the increase in pore pressure from the original hydrostatic value, and σ'_{vo} is the original in-situ vertical effective stress. Typically, the liquefaction ratio is considered to be limited to $0 \leq r_u \leq 1$. When $r_u = 0$, there is no EPP, and the soil is in its original condition. When $r_u = 1$, the EPP has risen to the value of the original effective stress. The effective stress is now zero, and the pore pressure is equal to the total stress. This is the maximum value of pore pressure if the soil body is to remain in vertical equilibrium; however, it has been suggested that $r_u > 1$ is possible for short periods of time, when the soil body does not remain in vertical equilibrium (Hughes and Madabhushi, 2018).

A useful framework to help understand liquefaction induced by cyclic loading is the Characteristic State model, proposed by Luong and Sidaner (1981). This model defines a linear Characteristic Line (CL) to separate regions of contractile and dilative behaviour on a plot of deviatoric stress (q) against effective confining stress (p') (figure 3). For relatively small q, in the subcharacteristic zone between the two CLs, the soil is contractile. For relatively large q, in the surcharacteristic zones between the CLs and the frictional Failure Lines (FLs), the soil is dilative.

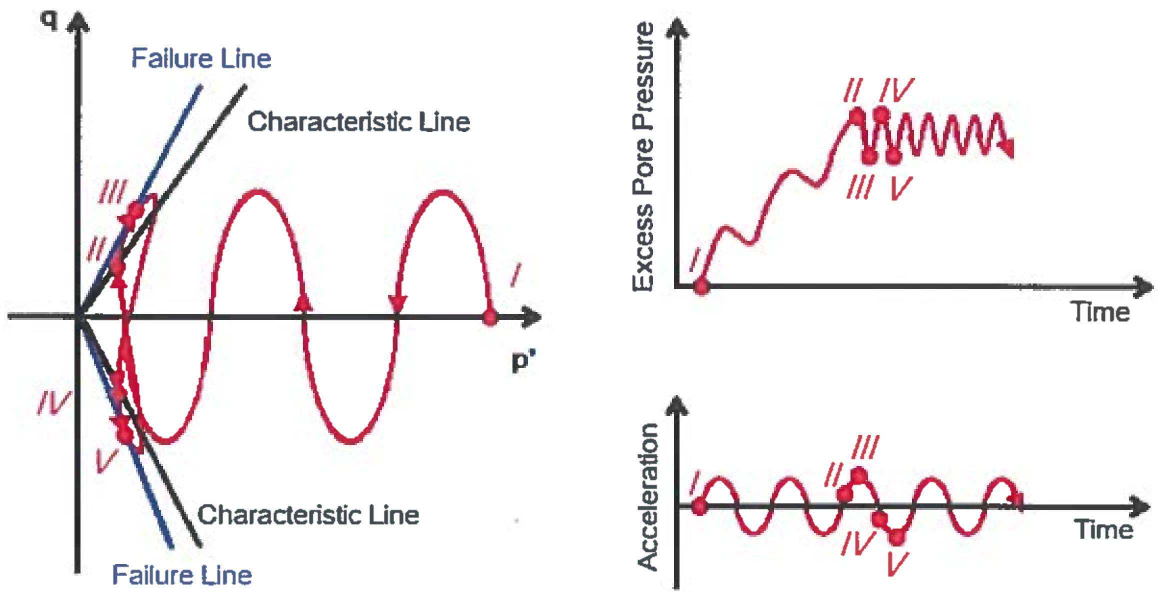

Figure 3: Liquefaction stress path for cohesionless soils under cyclic loading according to Characteristic State Theory (adapted from Chian, 2012, after Luong and Sidaner, 1981)

Treating the soil as undrained on short timescales, as cyclic shearing is initiated (I), the soil is contractile and p' falls as EPP rises. When the effective stress path crosses the CL (II), the soil begins to dilate, leading to an increase in p' and a fall in EPP. The stress path moves up the failure line until the direction of shearing is reversed (III), at which point it moves back through the contractile subcharacteristic zone, with a corresponding increase in EPP. The effective stress path then crosses the other CL (IV) and dilates up the FL until the shearing reverses again (V). This process then repeats, leading to the 'butterfly pattern' loops in the effective stress path observed by Ishihara et al. (1975). The 'butterfly' loops result in two cycles of contraction and dilation for every one cycle of applied shearing, leading to oscillations of EPP at twice the applied shearing frequency. A similar concept was developed by Ishihara et al. (1975), who identified a 'Phase Transition Line' separating regions of dilative and contracile behaviour.

2.2 Liquefaction Effects on Tunnels

The effects of soil liquefaction on a tunnel can be understood by considering the force mechanism shown in figure 4, from Chian and Madabhushi (2013). In the static condition, the soil's shear strength is mobilised on planes above the tunnel such that the resultant vertical component of force from the planes (F_{SP}) along with the overlying soil weight (F_{WS}) and the tunnel self-weight (F_T) are in equilibrium with the buoyant force (F_B). Should liquefaction occur, the resulting loss of shear strength will cause F_{SP} to reduce, and there will be an additional upwards force on the base of the tunnel from EPP (F_{EPP}). If pore pressures rise sufficiently, equilibrium will be lost, and the net upwards force will cause the tunnel to move upwards.

Chian (2012) introduced a Factor of Safety (FoS), which is a useful tool to assess the likelihood of tunnel floatation. It can be defined using the force components in figure 4 as:

$$FoS = \frac{F_{resist}}{F_{uplift}} = \frac{F_T + F_{WS} + F_{SP}}{F_B + F_{EPP}} \tag{2}$$

If during an earthquake FoS drops below 1, the forces driving uplift exceed those resisting it, so uplift is expected. One design approach is to ensure that FoS remains greater than one under the expected earthquake loading.

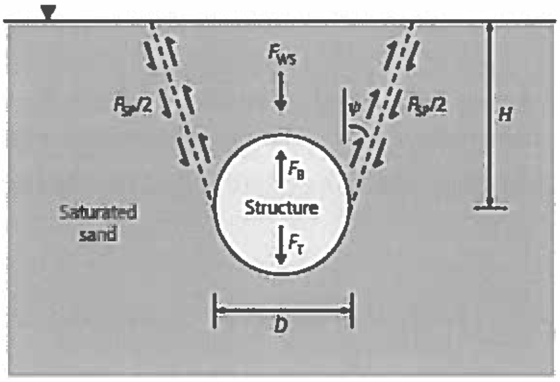

Figure 4: Force mechanism for tunnel uplift (from Chian and Madabhushi, 2013)

A FoS analysis can be useful to identify the commencement of uplift, but is unable to predict how quickly uplift progresses. Watanbe et al. (2016) comment that designing buried structures such that $FoS > 1$ throughout an earthquake may be overly conservative. Alternative design approaches allow uplift to begin by letting FoS fall below one, but ensure that subsequent displacement is limited so that the structure remains serviceable. Watanbe et al. (2016) propose a method to assess uplift potential by extending the semi-empirical Liquefaction Potential Index (P_L) introduced by

Iwasaki et al. (1978, 1982) to assess the potential for subsidence of surface structures following liquefaction.

P_L is computed by integrating one minus the liquefaction resistance ratio (F_L) with depth below a surface structure. Empirical evidence suggested that liquefaction beyond depths of 20 m (at field scale) did not influence subsidence, and the degree of liquefaction at shallow depths had most influence. Therefore a weighting function (w) was introduced that decreased linearly from the surface to a depth of 20 m and was zero thereafter (figure 5).

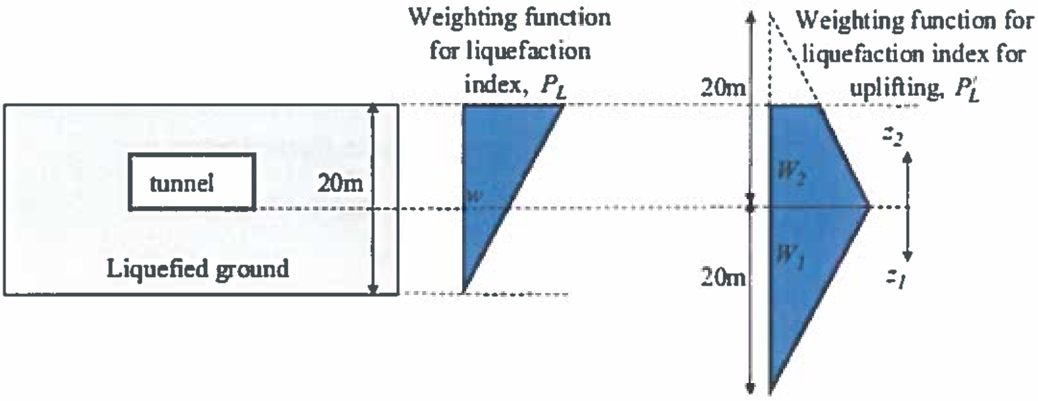

Figure 5: Weighting functions for Liquefaction Potential Indicies P_L and P_L' (from Watanbe et al., 2016)

Watanbe et al. (2016) extend this to the uplift of buried structures by considering the degree of liquefaction over a depth of 20 m above and 20 m below the structure, and identified that the degree of liquefaction close to the structure was most important. They define a Liquefaction Potential Index for uplifting (P_L') as:

$$P_L' = \int_0^{20} (1 - F_L) \cdot w_1 \cdot dz_1 + \int_0^{20} (1 - F_L) \cdot w_2 \cdot dz_2 \tag{3}$$

where the weighting functions are defined:

$$w_1 = 10 - 0.5z_1 \quad and \quad w_2 = 10 - 0.5z_2$$

where z_1 is positive downwards from the invert and z_2 is positive upwards from the invert.

F_L is the liquefaction resistance ratio, defined as the ratio between the Cyclic Resistance Ratio (CRR) and the Cyclic Stress Ratio (CSR). The CRR indicates the resistance of the soil to liquefaction and can be calculated from SPT-N data, CPT data, or triaxial test data. The CSR indicates the severity of shearing causing liquefaction and can be predicted if the design earthquake magnitude and site characteristics are known. After a review of several 1-g model tests, Watanbe et al. (2016) found a positive relationship between the value of P_L' and final uplift displacement, and suggest that a value $P_L' < 20$ will result in acceptably small uplift for cases when FoS falls below one. As the method has been calibrated by scaling from 1-g model tests, not geotechnical centrifuge and/or numerical models, there is some uncertainty around this threshold value of P_L'.

2.3 Previous MEng Projects

Five previous University of Cambridge MEng projects have been conducted in this area, all using 1-g shaking table testing with a window model box. Room (2014) investigated the effect of changing burial depth on the uplift of a rectangular tunnel, and concluded that increasing the burial depth reduced the tunnel uplift. EPP was measured at the tunnel invert and the far-field, and it was observed that pore pressures at the tunnel invert were generally lower than in the far-field. Jenkins (2015) conducted similar tests for the rectangular tunnel, and corroborated Room's results of decreasing uplift with increasing burial depth. PIV analyses were also conducted to visualise the soil deformation mechanisms. It was observed that soil moved from above the crown of the tunnel, down alongside the springings and in towards the invert as uplift progressed. The mechanisms became less pronounced as burial depth increased and total uplift reduced.

Wright (2016) and Bradley (2017) conducted tests with different pore fluid viscosities in order to investigate the effect of the hydraulic conductivity of the liquefiable layer on uplift. Wright conducted tests using the same rectangular tunnel as Room (2014) and Jenkins (2015) and proposed an exponential decay relationship between pore fluid viscosity and uplift. Meanwhile, Bradley conducted tests on a semi-elliptical tunnel and proposed a negative quadratic relationship between viscosity and uplift, with maximum uplift occurring for some intermediate value of viscosity.

Dhoru (2018) used the same semi-elliptical tunnel as Bradley (2017), but added vertical and horizontal fins to the tunnel invert in order to manipulate the soil-structure interaction and attempt to reduce the uplift. It was observed that vertical fins were more effective at reducing tunnel uplift, attributed to a combination of decreasing the EPP beneath the tunnel by isolating the invert soil from the surroundings, and increasing the soil-structure system stiffness. Whilst horizontal fins were able to resist the circular soil flows present in the uplift mechanism, they were overall less effective at reducing uplift.

2.4 Dynamic Soil-Structure Interaction

The presence of a buried structure can influence the behaviour of liquefied soil, which then influences the behaviour of the buried structure, leading to dynamic soil-structure interaction. Differences in EPP around an uplifting buried structure compared to the far-field were investigated with centrifuge testing by Chian and Madabhushi (2012) and numerical analysis by Chian et al. (2014). It was observed that EPP around the structure was significantly lower than in the far-field. This was attributed to suppressed dilation at the crown due to the uplift of the structure, large cyclic shearing of the soil at the springing of the structure leading to dilation, and a reduction in overburden stress at the invert as the structure rises. These observations of lower EPP suggest that the soil around the structure may retain some shear strength, and hence assuming full liquefaction of the soil in design may be conservative. Manipulating the reduction in EPP around the tunnel by varying its shape is one potential approach to remediating the uplift, as considered by Dhoru (2018).

2.5 Remediation

Schmidt and Hashash (1999) proposed that the following conditions must be satisfied for a tunnel to float:

1. wide-scale liquefaction of the surrounding soil;
2. the structure must have net buoyancy in the liquefied soil;
3. no foundations or additional structural components to hold-down the structure;
4. the liquefied soil must have the mobility to flow around the structure as it rises.

Potential approaches to mitigating uplift broadly fall into two categories. Conditions 2 and 3 above can be addressed by structural measures directly altering the buried structure. Meanwhile, conditions 1 and 4 can be addressed by ground improvement measures to the surrounding soil.

Structural Measures

A range of structural measures to improve the stability of pipelines in liquefiable soils are reported by Castagalia et al. (2017). Pre-cast bolt-on concrete collars can be used to increase the self-weight of a pipeline/tunnel to resist upwards EPP and buoyant forces (condition 2). However, the collars require careful design to ensure the overall unit weight of the collar-tunnel system is comparable to the surrounding soil, to avoid excessive subsidence of the pipeline/tunnel if liquefaction occurs. A further drawback of these schemes is that the increased mass of the tunnel could push the natural frequency of the soil-structure system down towards typical earthquake frequencies. Whilst uplift of the structure is prevented, damage could be caused by inertial forces from large vibrations at resonance during an earthquake. Screw-anchor systems consist of pairs of shafts with helical flights screwed into the soil either side of a pipeline, beneath the depth of the liquefiable layer, and connected by a strap over the top of a pipeline to restrain its buoyancy (condition 3). Careful design is required to ensure that the shafts extend far enough beneath the depth of the liquefiable layer to provide sufficient anchorage under the expected earthquake. They are unlikely to be adequate to restrain the uplift of a large-diameter tunnel.

Osbuto et al. (2016a) conducted 1-g shaking table tests on buried pipelines remediated against uplift by horn-like structures, which consist of a metal plate placed in a horizontal plane above the pipeline, and connected to it via a strut. This increased the area over which the buoyancy forces were distributed (condition 3) and was shown to be successful at reducing uplift. Osbuto et al. (2016a) also conducted 1-g tests which showed that flexible sheaths inserted into an existing pipeline were successful in preventing excessive flow of liquefied soil in to the pipeline, even if the joints of the original structure were damaged by differential uplift. Such a technique may help maintain the serviceability of pipelines if only small uplifts are expected, but would not be suitable if there is the potential for large uplift which may break the surface of the ground or for application to large-diameter tunnels.

Ground Improvement Measures

Madabhushi (2007) provides a general discussion on several ground improvement measures (condition 1) including: in-situ densification to reduce the contractile nature of a liquefiable deposit, column drains to drain away EPP, and grouting to provide a component of shear strength which is durable under earthquake loadings. Densification was considered in centrifuge tests by Chian and Madabhushi (2013) and found to be successful. This was attributed to reducing the degree of liquefaction (condition 1) and reducing EPP acting on the tunnel invert. In reality, densification may be possible for shallow buried pipelines but difficult for large-diameter tunnels, due to the considerable energy input needed and large effective stresses providing resistance to densification for depths beyond around 6 m (Madabhushi, 2019). Osbuto (2016a) investigated both drainage columns and chemical grouting in 1-g shaking table tests on pipelines and found they were successful; however, the effectiveness of the techniques was dependent on the drainage column placement/spacing of grout injections.

The use of granular fill material to remediate tunnel uplift has previously been considered. Whilst designing the seismic retrofit of the George Massey tunnel, Adalier et al. (2003) conducted centrifuge tests using densified-soil walls and high-permeability gravel walls either side of the tunnel (figure 6). Both remediation measures reduced uplift relative to the reference test (with no remediation), by preventing the flow of liquefied soil and pore fluid in behind the uplifting tunnel (condition 4). The gravel walls were particularly effective, reducing the uplift displacements virtually to zero. This was attributed to their ability to dissipate the build-up of EPP in the surrounding liquefiable soil, preventing the associated drop in strength (condition 1).

Chian and Madabhushi (2013) conducted centrifuge tests on a circular tunnel with coarse-grained back fill placed around the tunnel as shown in figure 7. Both forms of remediation were able to reduce the uplift of the tunnel compared to a reference test. The high permeability of the coarse back fill was able to quickly dissipate any EPP generated in the surrounding soil, reducing the degree of liquefaction (condition 1), so helping to retain shear strength in planes above the tunnel to resist its buoyancy. The inclusion of coarse-grained material around the sides and invert of the tunnel, as shown on the right of figure 7, was especially effective as any EPP acting on the tunnel invert was dissipated, reducing the upwards driving force. Despite the tests being conducted in window boxes, no PIV analyses of the uplift mechanisms were presented in this paper.

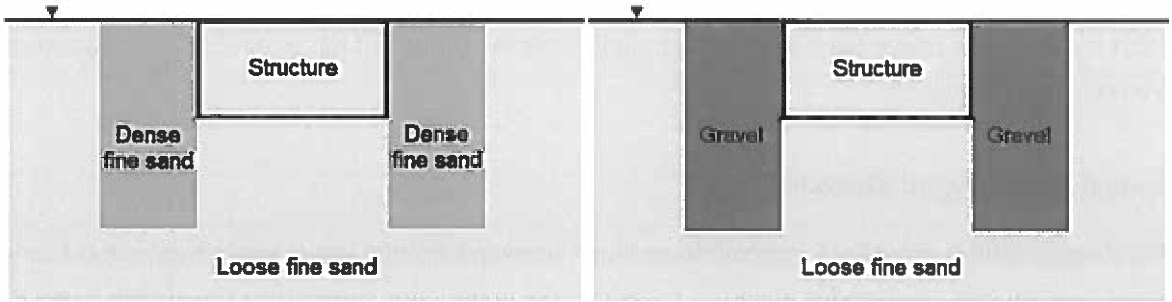

Figure 6: Remediation layouts investigated by Adalier et al. (2003) for George Massey tunnel

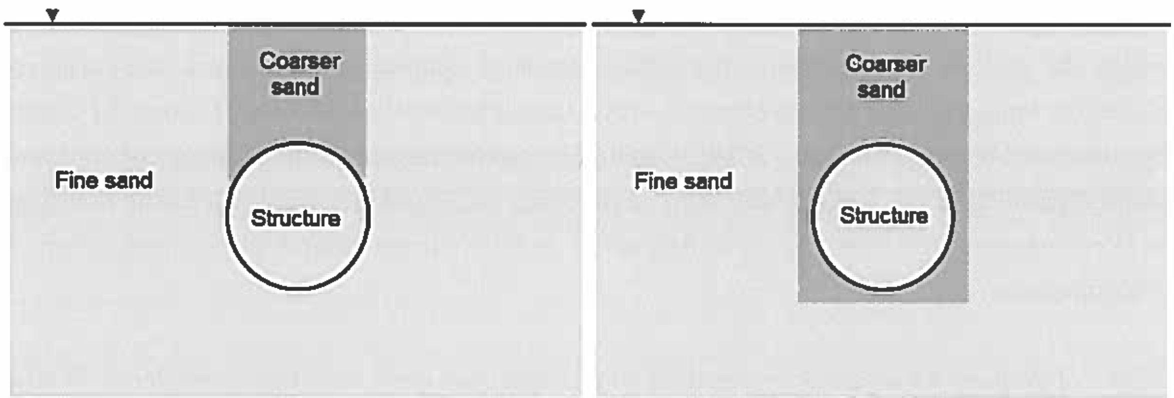

Figure 7: Remediation layouts investigated by Chian and Madabhushi (2013)

1-g shaking table tests on a circular pipeline conducted by Osbuto et al. (2016b) considered only one geometry of back fill replacement above and around the structure, similar to Chian and Madabhushi (2013), but varied the fill material including: compacted sand, crushed glass, crushed concrete, a mixture of tire chips and sand, and cement-treated liquefaction ejecta. Key requirements for material selection included ease of compaction, high hydraulic conductivity to drain EPP, and a similar unit weight to the in-situ soil to prevent excessive subsidence of backfill should surrounding soils liquefy. It was concluded crushed recycled glass had the best performance, as well as being a sustainable source of material.

This project intends to extend this work by considering further geometries of granular fill inclusions for a semi-elliptical tunnel, with PIV analysis to investigate how this remediation affects the uplift mechanism.

3 Experimental Methodology

3.1 Apparatus

Four small-scale model tests were conducted using the 1-g shaking table located at the Schofield Centre. A summary of the testing programme is included in table 1. The tunnel position shown for test 1 was consistent throughout the project; only the geometries of the granular fill were changed. Each model was subjected to a nominally sinusoidal earthquake input with a frequency (f) of 4.75 Hz, a displacement amplitude (d) of 4 mm and a duration of 6.5 $seconds$. This corresponds to an expected Peak Ground Acceleration (PGA) of:

$$PGA = (2\pi f)^2 d = (2\pi \times 4.75)^2 \times 0.004 = 3.56\ m/s^2 \ \ or \ \ 0.36g \tag{4}$$

where $g = 9.81\ m/s^2$. It was observed in experimental results that the shaking table did not apply a perfect sinusoidal input, and the presence of significant frequency components at the third and fifth harmonics resulted in an actual input PGA of $0.6g$ (see section 6).

The models were prepared in a box with internal dimensions of $700 \times 300\ mm$ in plan and 500 mm height. One wall of the model box was made from transparent Perspex to enable the soil deformation to be observed. The Perspex window was highly polished at the start of the project to remove any scratches which could cause errors in subsequent PIV analysis. Control markers consisting of a white circle with a black backing made from vinyl stickers were applied to the Perspex window in a regular pattern to enable photogrammetic corrections of the video frames to be made during the PIV analysis (see section 3.5).

The tunnel model used was made and used by Bradley (2017) and used by Dhoru (2018). This was semi-elliptical in section with dimensions as shown in figure 9. The flat invert of the tunnel aided consistent placement when constructing models. The tunnel was constructed from 3D-printed PLA plastic with PTFE end caps. The PLA tunnel shell was highly porous, therefore the inside was filled with closed-cell foam and the exterior was coated with several layers of varnish and Plastidip to minimise pore fluid ingress. Some pore fluid ingress during saturation was inevitable, therefore the tunnel was weighed quickly after every test to ensure accurate tracking of the tunnel's mass. When placing the tunnel into the model container, the PTFE end caps where lubricated using silicone grease to prevent sand entering the gaps between the tunnel and the container, and to minimise friction against the walls which would violate the assumption of 2D plane-strain conditions.

Table 1: Testing Programme

Test	Layout	I_D	Objective
1	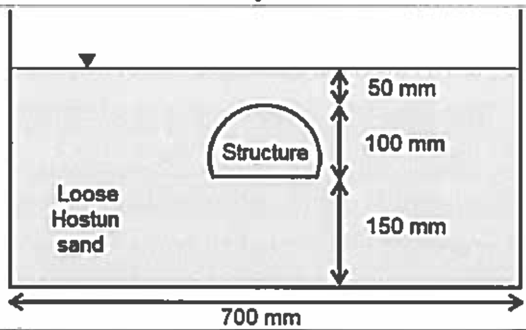	37%	Establish experimental procedure. Provide a reference against which to evaluate subsequent remediation attempts.
2	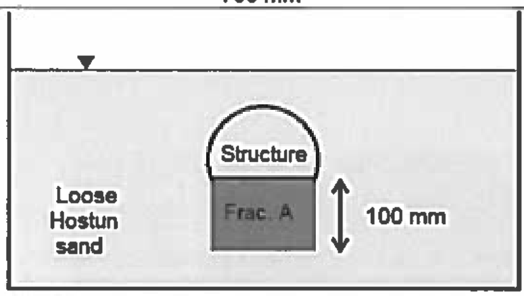	46%	Investigate the effect of a block of coarse-grained granular fill placed beneath the tunnel invert for a depth of 100 *mm*.
3	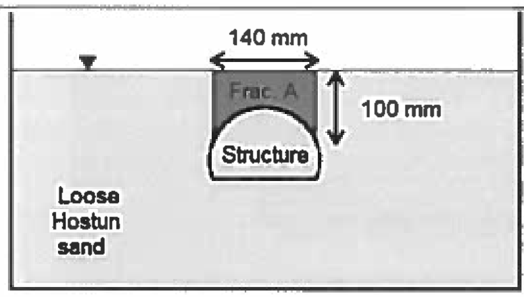	32%	Investigate the effect of a block of coarse-grained granular fill, of one tunnel width, placed above tunnel.
4	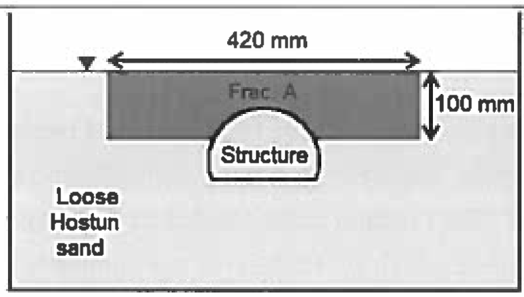	33%	Investigate the effect of a block of coarse-grained granular fill, of three tunnel widths, placed above tunnel.

3.2 Model Preparation

The liquefiable layer in each model was formed from Hostun sand (properties given in table 2) for consistency with previous MEng projects. The Hostun sand was poured manually from a suspended hopper to a target relative density (I_D) of 35%. This was sufficiently loose to allow liquefaction to occur on shaking. Before constructing the models, trial calibration pours into a container of known volume were conducted and it was determined that a drop height of 200 *mm* and a 16 *mm* diameter nozzle aperture gave the desired I_D. The direction of pouring was alternated between lateral and longitudinal sweeps for each layer to improve homogeneity. The actual I_D achieved in the liquefiable layer for each model is reported in table 1. Some inconsistency is inevitable with the manual pouring technique. An error whilst preparing test 2 resulted in the Hostun sand being poured to I_D of 70 %. Limited availability of the test rig meant there was only enough time to excavate to tunnel invert level and re-pour the upper layer in a loose state, rather than fully re-pouring. The high I_D of this foundation layer must be considered when comparing the results of test 2 to other tests.

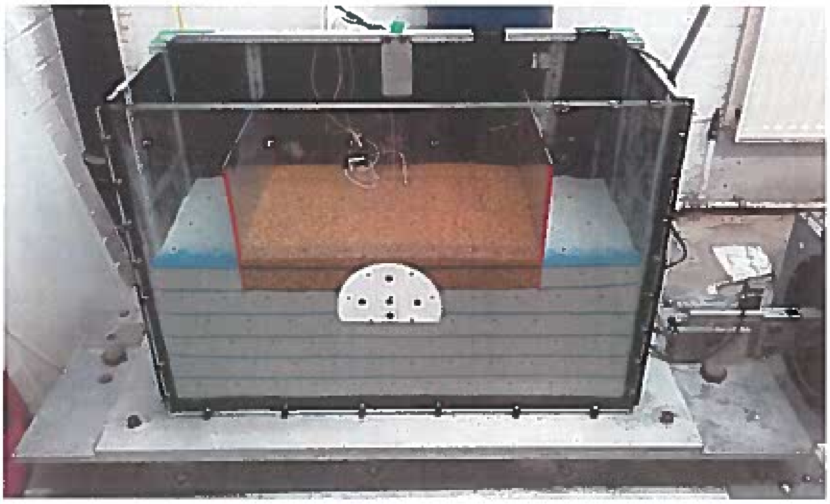

Figure 8: Example of model preparation *(for test 4)*

The granular fill inclusions in models 2 - 4 were formed from Leighton Buzzard Fraction A sand. This material was selected due to its high hydraulic conductivity relative to the Hostun sand (table 2), which allowed it to rapidly drain away EPP. The Fraction A was placed in thin layers by hand with a large drop height and low flow rate to achieve a high I_D. Each layer was compacted to further increase I_D and prevent liquefaction. The very uniform grading of the sand (C_u = 1.27, from table 2) meant only a small compacting effort was required. This was beneficial as it avoided compacting the surrounding areas of loose Hostun sand. Metal shutters were used where appropriate to separate the two materials whilst preparing the models (figure 8).

All models were saturated with water from a header tank via porous saturation tubes in the base of the model. The head of water was kept small through the saturation to prevent piping failure in the soil. In each case, the water level was brought several centimetres above the upper surface to eliminate any capillary suction, and then reduced to just above the surface to avoid large waves forming during shaking which could disturb the soil surface. Due to lack of suitable apparatus, the models were not saturated under vacuum as is the norm for geotechnical model preparation. This meant it was inevitable some air bubbles would be trapped in the model, limiting the degree of saturation that could be achieved.

To aid the PIV tracking, a portion of the Hostun sand was dyed with blue ink and mixed in a ratio 1:2 blue:white to enhance the visual texture. The Fraction A sand was not dyed as it already had sufficient visual texture. During pouring, blue bands of sand were placed across the model at height intervals of 40 mm, to allow corroboration of the PIV outputs by inspection of the video frames (see figures 22a - 25b)

Table 2: Soil material properties

Property	Symbol	Hostun Sand	Fraction A Sand	Units
Specific Gravity	G_s	2.65 [a]	2.65 [d]	-
Critical state friction angle	ϕ_{crit}	33 [a]	39 [d]	*degrees*
Maximum void ratio	e_{max}	0.101 [a]	0.83 [d]	-
Minimum void ratio	e_{min}	0.555 [a]	0.55 [d]	-
Coefficient of uniformity	C_u	1.67 [b]	1.27 [d]	-
Coefficient of curvature	C_c	0.98 [b]	1.12 [d]	-
d_{10} size	d_{10}	0.21 [c]	1.27 [d]	mm
Hydraulic Conductivity	K	4.4×10^{-4} [e]	1.6×10^{-2} [e]	m/s

[a] Data from Mitrani (2006).
[b] Data from Heron et al. (2014)
[c] Data from Chian et al. (2014)
[d] Data from Rouhanifar et al. (2014)
[e] After Hazen (1911): $K\ (m/s) \cong 0.01 \times d_{10}^2\ (mm)$

3.3 Data Acquisition

The instrument layout placed in the models is displayed in figure 9. All sensors were placed in the mid-plane of the model. Wires were routed as close to the mid-plane as possible to reduce the potential impact of local high hydraulic conductivity drainage paths along the surface of the wires impacting on global behaviour. Micro-Electro-Mechanical System (MEMS) accelerometers were placed on the tunnel springings to measure vertical accelerations and at the tunnel crown to measure horizontal accelerations. The MEMS were attached directly to the rigid shell of the tunnel before any flexible waterproofing layers were applied to avoid damping of the acceleration readings. Despite the waterproofing, the vertically-aligned MEMS failed repeatedly due to water ingress or connection failure; little useful data was collected. The shaking table input was measured with a MEMS accelerometer and a Linear Variable Differential Transformer (LVDT). The uplift displacement of the tunnel was measured via a Draw Wire Potentiometer (DWP) attached to the crown.

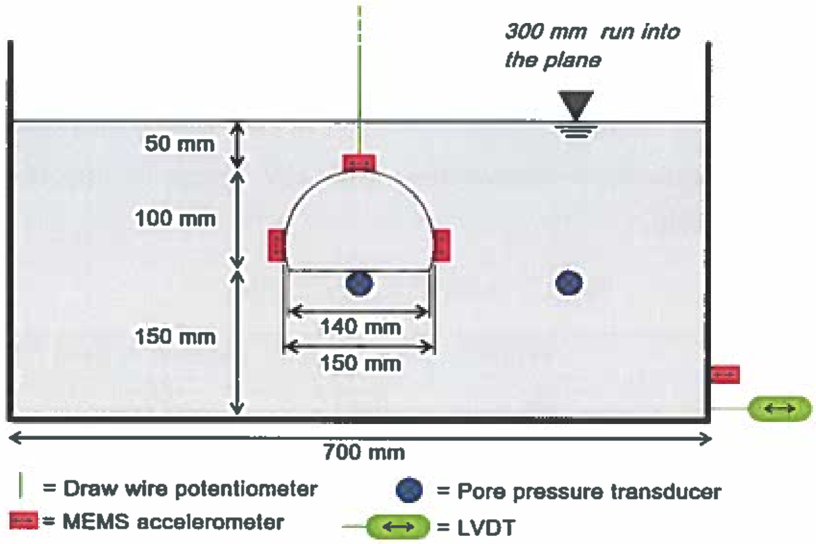

Figure 9: Instrument layout for model testing

Pore pressures were measured using Pore Pressure Transducers (PPTs): one attached to the tunnel invert, and one placed in the far-field at the same depth, equidistant from the tunnel and the box wall. Both PPTs were placed with their axes perpendicular to the shaking direction to avoid recording hydrodynamic pressures. For test 1, a 7 *bar* and 3 *bar* PPT were used for the invert and far-field respectively. For subsequent tests, a 350 *mbar* and 1 *bar* PPT were used.

Prior to each test, all instruments were calibrated against known physical quantities to obtain a relationship between physical measurement and voltage output. When placing instruments in the models, care was taken to ensure that they would remain within the linear region of their range as far as possible. During testing, all instruments were sampled at a rate of 1000 *Hz* using DASYLab datalogging software.

All tests were filmed through the Perspex window using a GoPro Hero 5 camera. Trial videos were taken before the beginning of testing to determine the best camera settings. Resolution was set to 2.7K (2704×1520 *pixels*) and 60 frames-per-second, as this presented the best trade-off between image quality and sample rate (12 frames per earthquake cycle). The lens adjustment was set to 'linear field of view' to minimise 'fish-eye' distortion from the GoPro wide-angle lens. The shutter speed was set to $1/120\ s$, as this gave the best compromise between image quality and minimising blur of the moving box.

As the shutter speed was very fast, the models were brightly lit with several LED lights to increase image quality. These lights should have provided a steady light source from DC power, but some flickering was noticed, most likely due to a poor quality rectifier in the driving circuit. As the frame rate ($60\ Hz$) was close to the mains supply frequency ($50\ Hz$), trial videos were taken to check that the effect of flickering on image quality was not excessive.

3.4 Data Processing

Post-processing of data was undertaken using MATLAB software. Calibration factors were applied to the data to transform instrument voltage readings to physical quantities. All data was low-pass filtered using a 12^{th} order Butterworth filter with a cut-off frequency of $40\ Hz$ (figure 10). This filter was selected to attenuate high frequency noise from the data whilst minimising attenuation in the pass-band. The filter was implemented using the MATLAB *filtfilt* function, which passes the data through the filter in both the forwards and reverse directions. This has the advantage of preventing any phase distortions and doubling the order of the filter (MathWorks, 2019).

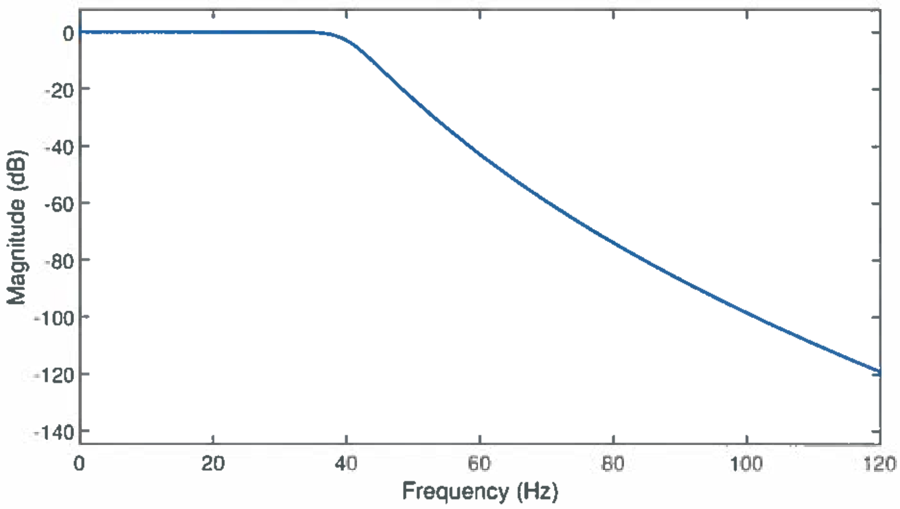

Figure 10: Frequency-Magnitude Response of filter employed

The pore pressure data from the invert PPT was post-processed to eliminate hydrostatic pressure drift during the tunnel uplift. As the PPT was attached to the invert, this could be achieved using the DWP uplift data as follows:

$$EPP_{invert,\ adjusted} = EPP_{invert,\ original} + \gamma_w \cdot \delta_{uplift}$$

An example of the effect of this adjustment is shown in figure 11.

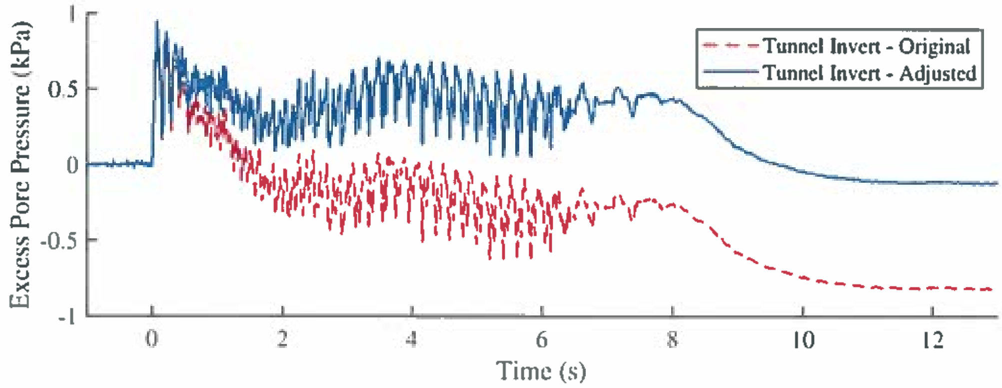

Figure 11: Effect of removing hydrostatic drift from measurements of EPP at tunnel invert *(Example from Test 3)*

3.5 Particle Image Velocimetry

Geotechnical Particle Image Velocimetry (GeoPIV) software was used to track the deformations of the soil during the tests. The basic operation of the software is explained through figure 12, after White and Take (2002). Each frame is split into a series of small test patches (say, 40×40 *pixels*). The software then attempts to 'search' for each patch in the subsequent frame by correlating the visual texture in the patch (i.e. the spatial variation in brightness) with positions within a pre-defined search area. The position of the peak on the correlation plane indicates the displacement of that patch of soil between the two frames. This is repeated for many patches across each frame of the video to build up an image of the deformation mechanism of the soil. The software was also used to track markers placed on the end caps of the tunnel, to provide extra displacement data to support the DWP readings.

The software version used in this investigation was *GeoPIV_RG*, which presents several advantages over previous versions, including Reliability-Guided (RG) methods to improve computational efficiency and the ability for first-order subset deformation to improve accuracy of correlations (Stanier et al., 2015).

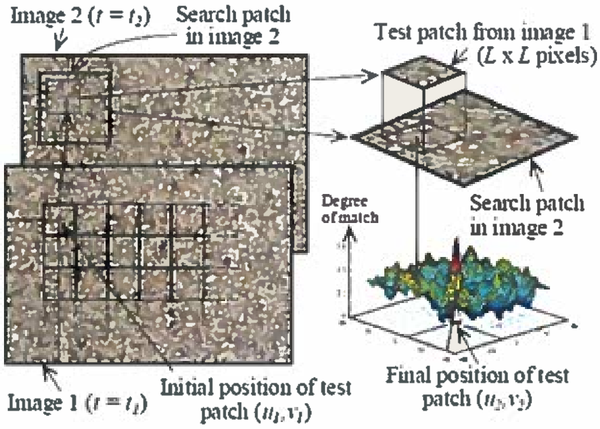

Figure 12: Principles of PIV (White and Take, 2002)

A photogrammetric correction was performed on the output of each PIV analysis. A Mylar card calibration was used to accurately determine the distances between the control markers on the Perspex window. These markers were then used to transform the displacement fields from UV image-space (in units of *pixels*) to XY object-space (in units of *mm*). This eliminates the effects of any distortion from the camera lens and removes the overall motion of the model box, giving only the displacements of the soil relative to the box. An example raw object-space output from Test 4 is shown in figure 13a. Any erroneous data (termed 'wild vectors') was removed manually (figure 13b), and the displacement field replotted after linear interpolation over a regular grid of points (figure 13c).

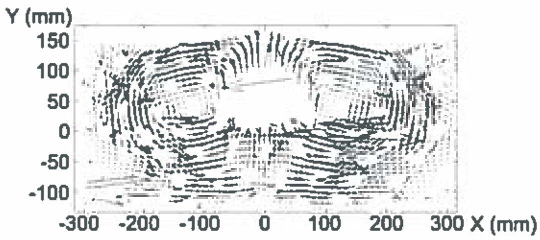

Figure 13a: Raw PIV output

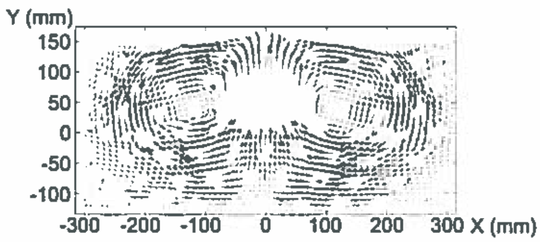

Figure 13b: PIV output with wild vectors removed

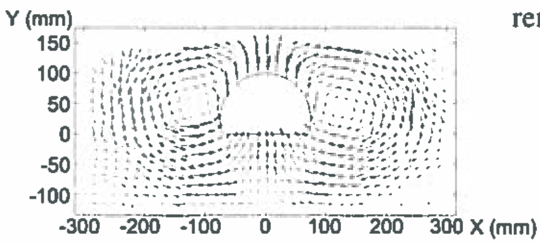

Figure 13c: Interpolated PIV output

4 Tunnel Displacement Response

4.1 Tunnel Uplift

The uplift displacement responses for each test measured with the potentiometer are displayed in figure 14. In each case, uplift begins rapidly after the onset of shaking at time zero and tends to decrease in rate as the earthquake progresses.

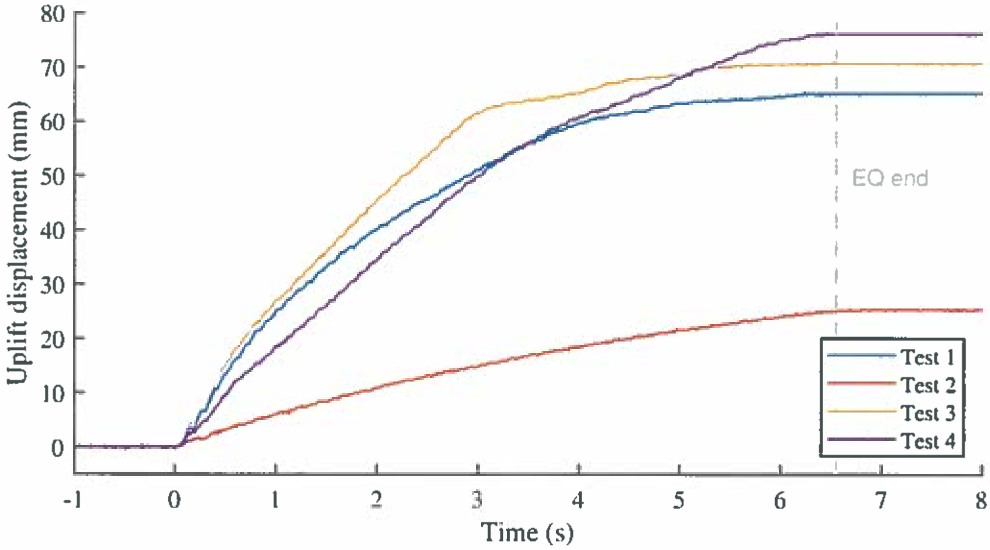

Figure 14: Tunnel uplift responses from potentiometer measurements

There is a stark contrast between the behaviour of tests 1, 3 and 4 (with no remediation or remediation above the tunnel) and the behaviour of test 2 (with remediation below the tunnel). During tests 1, 3 and 4, the tunnel uplifted through the original ground surface (uplift > 50 *mm*) with final uplifts of 65 *mm*, 71 *mm* and 76 *mm* respectively. Meanwhile during test 2, the tunnel remained buried with a final uplift of 25 *mm*.

There are also differences in the shape of the uplift curves. During tests 1 and 3, the uplift rate drops rapidly and falls almost to zero before the end of shaking at 6.5 *s*. This is due to the tunnel uplifting through the surface of the model, seen in figures 22b and 24b. From Archimedes' principle, the buoyant force on the tunnel is equal to the weight of liquefied soil it displaces. As the tunnel rises above the surface, it displaces less liquefied soil below the surface. The buoyant force driving uplift decreases and the tunnel reaches a new static equilibrium at the surface. In tests 2 and 4, there is steady uplift throughout the earthquake, with a gradually decreasing rate, until the uplift stops abruptly with the end of shaking at 6.5 *s*. This is despite the continued presence of high EPP at the invert and in the far-field for several seconds after the end of shaking (figures 19 and 20). This implies that the uplift behaviour is more complex than that of simply a buoyant object in a heavy viscous fluid, for which further uplift would be expected whilst EPP was high enough to maintain a large degree of liquefaction throughout the model. This is consistent with the observations of Chian et al. (2014) that the earthquake input itself, as well as the presence of high EPP, has an important influence on uplift.

As discussed above, for tests 1, 3, and 4 the final uplift value will be sensitive to mass of the tunnel, which determines the level it will float on the surface so equilibrium is reached. The mass of the tunnel varied between tests due to different amounts of water ingress during saturation, and different masses of soil being carried up on the crown of the tunnel following generation of negative EPP after clearing the water table (seen in figures 22b, 24b and 25b). Therefore the final uplift displacements have limited value, and in all cases are well beyond the point of failure. Of more interest is the uplift behaviour over the first seconds of the earthquake. The tunnel in test 2 shows a considerably lower rate of uplift than all other tests, which suggests that granular fill placed below the tunnel is most effective at mitigating uplift. However, it must be noted that for an existing tunnel this would be the most difficult retrofit measure to implement. For a new-build tunnel, this scheme would be more appropriate.

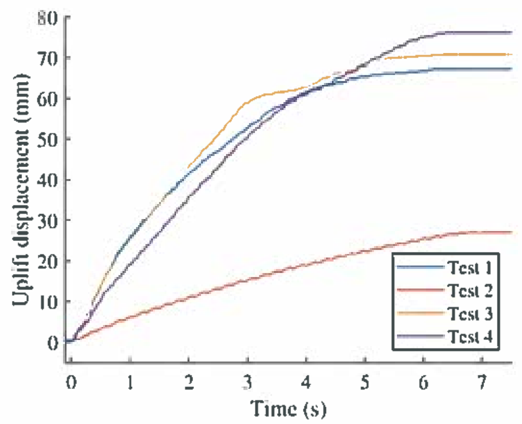

Figure 15: Tunnel uplift responses from PIV tracking

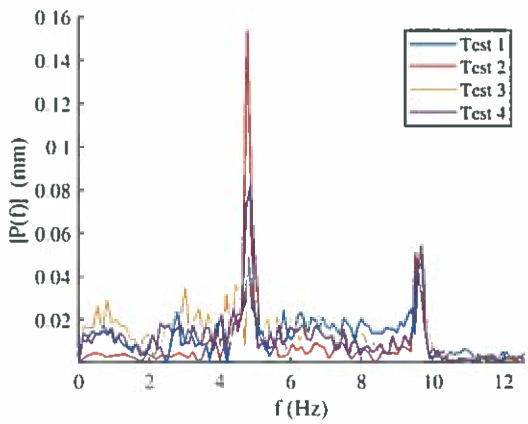

Figure 16: Tunnel uplift spectra from PIV tracking

The strong cyclic components of uplift at the input frequency and second harmonic observed in previous investigations (particularly Jenkins, 2015, and Dhoru, 2018) were not seen in any of the uplift responses in figure 14. This may be an effect of using a potentiometer to measure the uplift; it responsiveness to dynamic effects depends on the stiffness of the torsional spring to tension the draw-wire, which may have degraded. The tunnel uplift displacements were also found by tracking the markers on the tunnel end caps, and are displayed in figure 15. These results display a clearer cyclic component to the uplift response. The frequency spectrum plotted in figure 16 (with monotonic components of uplift eliminated) shows strong cyclic contributions at the earthquake input frequency and the second harmonic, which is consistent with the observations of Dhoru (2018). This suggests there is a periodic variation in the net force driving uplift on the tunnel, which is likely to arise from the cyclic nature of the EPP acting on the tunnel invert discussed in section 5. It also suggests that the nature of the uplift mechanism must change over the course of a cycle to facilitate this varying rate of uplift. This is explored further in section 7.

4.2 Tunnel Rotations

PIV tracking of the tunnel end cap markers was also used to determine the rotations of the tunnel about its axis over the course of shaking, shown in figure 17. Figures 22b, 23b, 24b and 25b in section 7 show the final position of the tunnel. The tunnel displays a rocking response in all of the tests. The tunnel has a net anticlockwise rotation in all tests except test 2, which rotates clockwise. Tests 1, 2 and 4 undergo similar magnitudes of total rotation at around 2°. Meanwhile the rotation in test 3 is much greater, with a final value of -15.3°. A significant proportion of this rotation occurs after 4 s of shaking, following a small plateau between 3 s and 4 s. Figure 14 shows this is after nearly all the uplift of the tunnel has occurred. Close inspection of the video of test 3 indicates this extra rotation is caused by the discharge of pore water and air bubbles from a void beneath the invert up the right-hand side, which destabilises the tunnel as it sits on the surface and causes further rotation.

The frequency spectrum of the rotations shown in figure 18 indicates that the cyclic component of the rotations is almost entirely at the input frequency. This would suggest that there is an asymmetric nature to the uplift mechanism that is causing these rotations, with a dependence on the direction of the input ground accelerations. The rocking of the structure may influence the deformation mechanism by varying the distribution of stresses around the tunnel through soil-structure interaction effects. The strongest rocking response is seen for test 2, with the largest peak-to-peak rotation amplitude in figure 17b and the largest cyclic component in figure 18. Inspection of the video of test 2 suggests that the nature of the uplift mechanism that forms due to the presence of the granular fill block at the invert may cause this strong rocking. Further investigation into the uplift mechanisms is conducted in section 7.

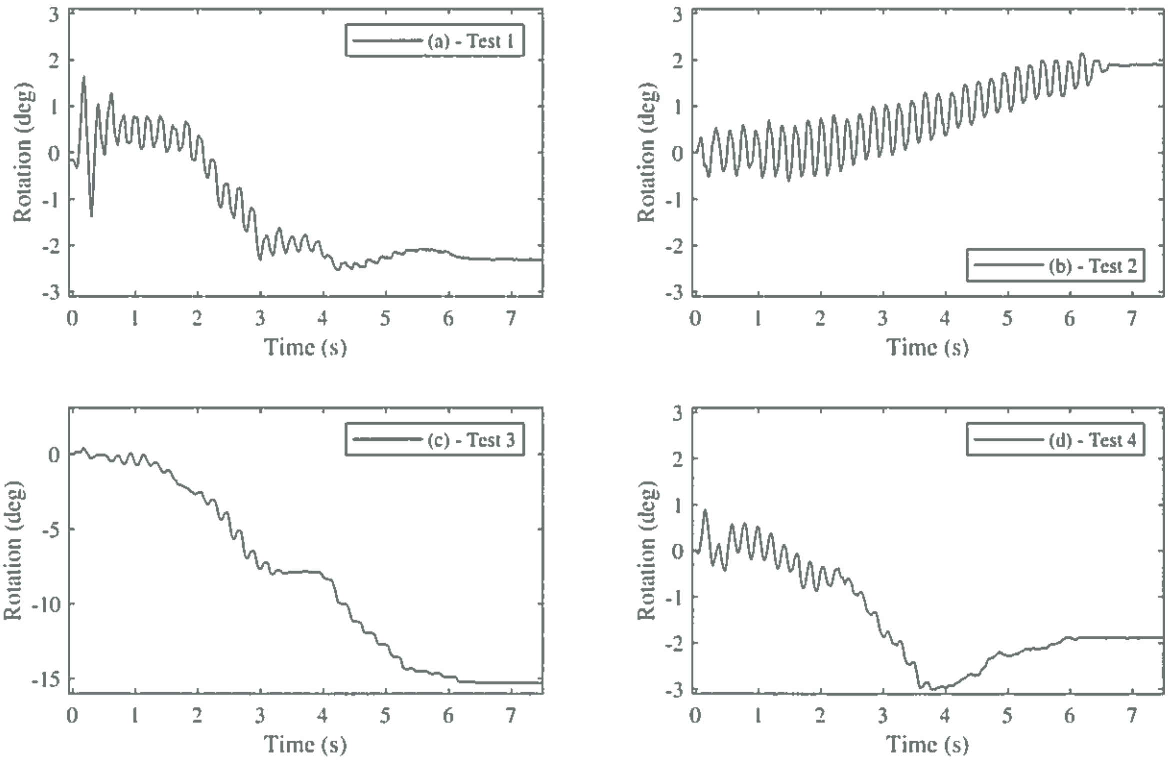

Figure 17: Tunnel rotation responses from PIV tracking

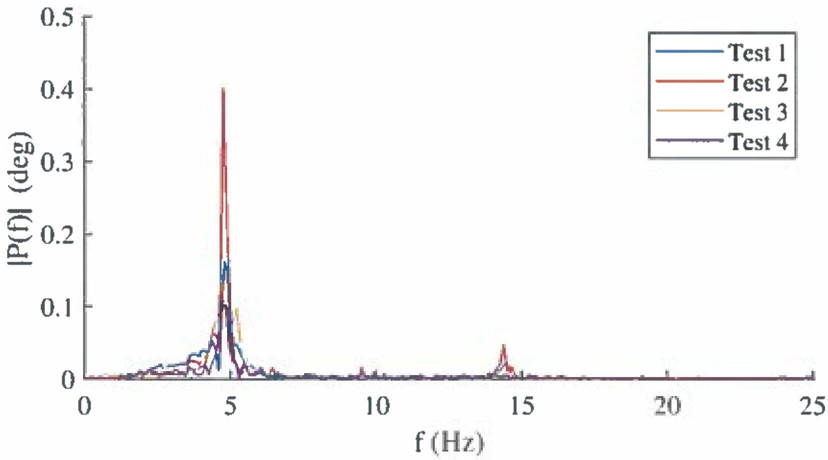

Figure 18: Tunnel rotation spectra from PIV tracking

5 Excess Pore Pressures

The EPP time histories measured at the tunnel invert are displayed in figure 19, after being adjusted for hydrostatic drift as discussed in section 3.4. In test 1, a 7 *bar* PPT was used to measure EPP. Observed EPP was less than 1 *kPa* which corresponds to only 0.14% of the instrument's range. The cyclic component has been lost due to the poor signal-to-noise ratio, but variations in average can still be seen. For subsequent tests, a 350 *mbar* PPT was used which gave higher resolution.

In all cases, the EPP at the invert is lower than that seen in the far-field. This is due to the reduction in overburden stress at the invert as the tunnel rises, as discussed by Chian and Madabhushi (2012) and Chian et al. (2014). Chou et al. (2011) indicated that this results in a hydraulic gradient being established from the far-field towards the invert, which draws liquefied soil and pore fluid towards the invert creating the uplift mechanisms seen in section 7. Tests 1, 3 and 4 display similar behaviour, with a sharp rise in EPP over the first cycle, which acts to destabilise the tunnel. The EPP then reduces as the shaking continues and the tunnel uplifts. In test 2, the average EPP over the first cycle is actually negative, suggesting there has been dilation in the compacted Fraction A sand or in the dense foundation layer. This suction reduces the initial uplift of the tunnel. The EPP then settles to a steady response with larger peak-to-peak amplitudes but the lowest average at 0.2 *kPa*. The lower EPP acting on the invert is likely to contribute to the reduced uplift seen in this test.

Tests 1, 2, and 4 show an increase in EPP at the end of shaking after 6.5 *s*. When the tunnel stops uplifting promptly after the end of shaking, the overburden stress beneath the tunnel will increase, therefore the EPP will increase. There will also be a short continued flow of pore fluid from the far-field towards the invert due to the hydraulic gradient, until the EPP equalises. This increase in EPP is not seen clearly in the EPP trace for test 3, as the tunnel has already stopped significantly uplifting before the earthquake ends (figure 14). Re-consolidation then occurs, with tests 1, 2 and 3 showing pore pressure equalisation around 4 *s* after the end of shaking. Test 4 shows a rapid drop in EPP, within 1 *s*. This is due to fast re-consolidation of the soil underneath the tunnel through the high hydraulic conductivity drainage path offered by the subsided granular fill (figure 25b).

The EPP time histories measured in the far-field are displayed in figure 20. All tests show similar trends, with EPP rising at the onset of shaking and oscillations ending quickly after the end of shaking, before re-consolidation takes place over several seconds. Tests 1 and 3 show similar behaviour, with EPP building up rapidly within a few cycles of shaking and the mean value quickly reaching the value for $r_u = 1$, indicating full liquefaction. In both cases, particularly test 3, the average value of EPP exceeds the value for $r_u = 1$ as shaking progresses. This is due to the PPTs being drawn

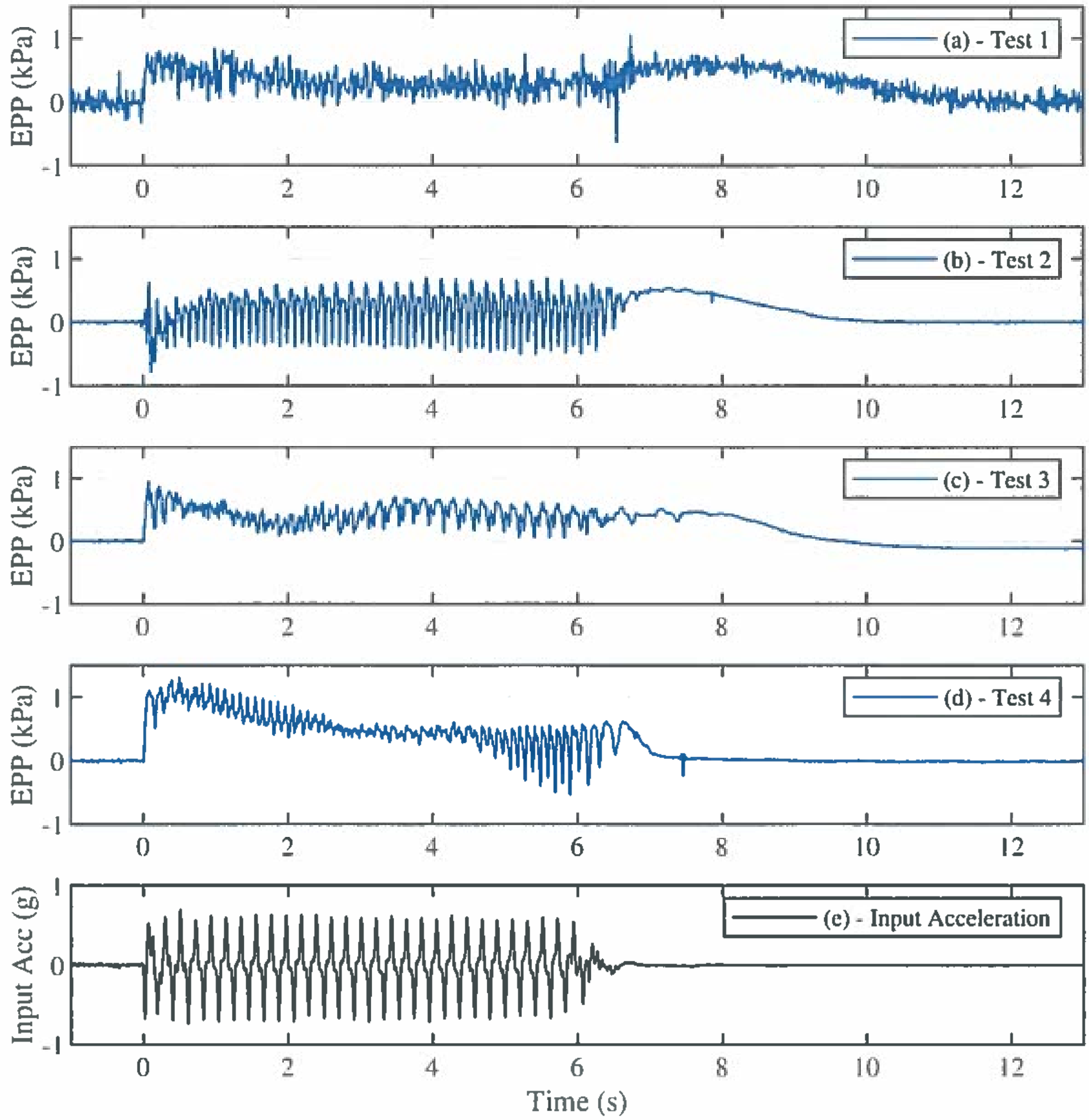

Figure 19: Excess pore pressure at tunnel invert

downwards as the soil deformation mechanism forms, resulting in a drift in the hydrostatic pressure. The change in hydrostatic head at the end of shaking for tests 1 and 3 is in agreement with the drop in height of the PPT positions measured when dissecting the models after testing.

Test 4 also shows a change in hydrostatic head over the course of shaking of 190 *mm*. This is far greater than the measured PPT height change of 52 *mm*, which suggests this PPT has failed during the test as the calibration factor has drifted. This PPT also shows a complete suppression of the cyclic component of EPP after 4 s of shaking. This could be due to instrument failure or the migration of air bubbles up through the model as observed in the test video, which could heavily damp oscillations in pore pressure. Test 2 shows different behaviour to the other tests. The EPP quickly rises to the value for $r_u = 1$ and maintains a steady value until 1.5 s, when the average value begins to fall and the peak-to-peak amplitude increases. This suggests the soil is re-consolidating during the course of shaking, leading to stronger shear-induced dilation and contraction over each cycle. This could be due to pore water being drawn into the denser foundation layer as it dilates during shearing, or pore water being drawn towards the large void that forms beneath the invert in this test (figure 25b). Test 2 also takes less time to fully re-consolidate than tests 1 and 3, as there will have been less pore water expelled upwards from the dense foundation layer in test 2 than the loose foundation layers in the other tests.

Spectral analysis of the EPP time histories indicates that the oscillations in EPP at the invert occur at double the input frequency. This is consistent with the expectations of Characteristic State theory introduced in Section 2.1. At the invert the confining stresses are low, due to the low unit weight of the tunnel, but the cyclic shear stresses will be large due to relative movement between the tunnel and soil. Hence it is likely the effective stress path will cross both CLs during every earthquake cycle leading to two cycles in EPP. Meanwhile, the spectrum of the EPP in the far-field indicates that oscillations of EPP were dominated by components at the input frequency, which appears to contradict the Characteristic State theory. PIV analysis of the soil deformation mechanisms (figures 26 to 29) show that at the far-field PPT location, there is a net movement of soil towards the tunnel invert. This could result in a static component of shear stress towards the invert at this point. Therefore the effective stress path on the $q - p'$ plane will no longer be centred on the p' axis as shown on figure 3, and instead will drift in the direction of increasing q. If the magnitude of the static component of q is significant compared to the amplitude of the cyclic component of q, the effective stress path will only cross one of the CLs during each cycle of shaking. The full 'butterfly' loops will not form, and only one cycle of EPP oscillation will occur for every input cycle.

An alternative cause of the input-frequency oscillations in far-field EPP could be changes in the total stress state in the soil due to inertial forces as the soil accelerates around the flow paths seen in the soil deformation mechanisms (section 7). It can be seen in figure 20 that the far-field EPP peaks regularly exceed the value required for full liquefaction ($r_u = 1$) in all tests. This suggests that the soil body is not remaining in vertical equilibrium, as the pore pressure begins to exceed the static total vertical stress (Hughes and Madabhushi, 2018). The spectral analysis of the far-field EPP reveals that for tests 1, 3 and 4, the EPP oscillations were heavily dominated by components at the input frequency with little contribution from the second harmonic. In test 2, components at

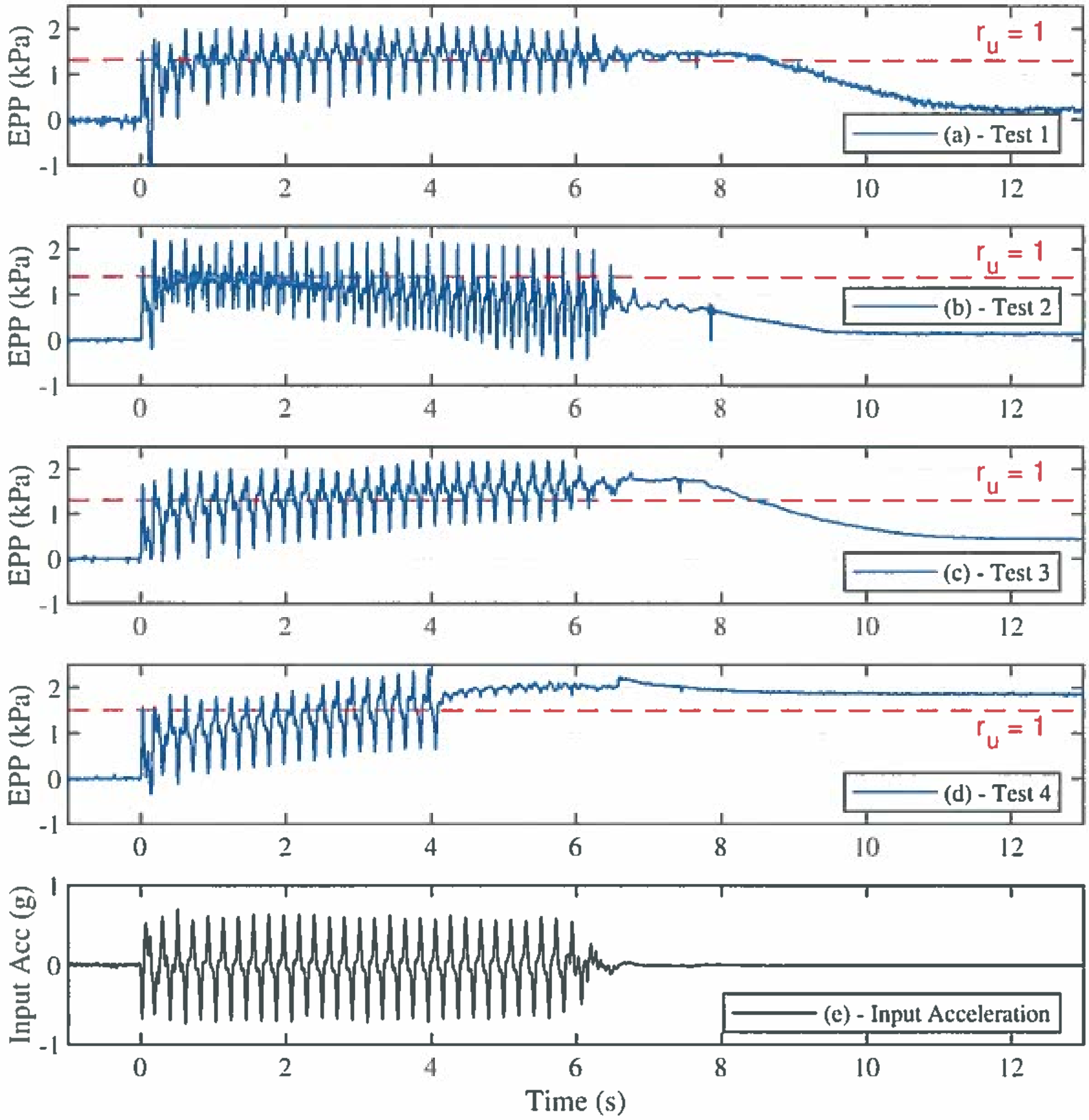

Figure 20: Excess pore pressure in far-field at initial tunnel invert depth

the input frequency and second harmonic were comparable. Analysis of the sub-cyclic soil deformations (section 7.2) shows that the direction of soil flow around the PPT changes with every half cycle. This results in a change in total stress every half cycle, which if the soil remains undrained, causes input-frequency oscillations in EPP. In tests 1, 3 and 4, there is very significant circular flow of the liquefied soil (figures 26, 28, 29) whilst test 2 showed little flow of liquefied soil around the far-field PPT (figure 27). This appears to relate to the relative importance of the input-frequency component in the spectrum.

6 Horizontal tunnel accelerations

Horizontal acceleration time histories for the shaking table input (i.e. bedrock motion) and the tunnel crown are plotted in figure 21. It can be seen the actual input PGA in each test ranged between $0.6g$ and $0.7g$, larger than the prediction in section 3.1, due to the shaking table not applying a perfect sinusoidal input. For all tests, the tunnel accelerations are dominated by frequency components at the input frequency, and little phase lag between the tunnel and the input is seen.

In test 1, the horizontal accelerations of the tunnel were greater than the input accelerations throughout the earthquake. This suggests that there has been a resonant response with the natural frequency of the tunnel-soil system lying close to the input frequency. It has not been possible to predict the natural frequency of the system, as the available correlations for soil stiffness are not valid at the low confining stresses encountered in 1-g testing.

In test 2, the accelerations of the tunnel remain fairly constant throughout the earthquake with peak values around 60% of the input PGA. This suggests a significant degree of isolation between the tunnel and the input motion. The ground improvement applied beneath the tunnel has been able to increase the stiffness by reducing the degree of liquefaction, however the soil around the tunnel can still liquefy strongly. This results in a low shear stiffness that is not able to effectively transfer input accelerations to the tunnel.

Tests 3 and 4 show similar behaviour, with an increase in the magnitude of the peak tunnel accelerations over the course of shaking. This is in contrast to the observations of Dhoru (2018), who saw in several tests that the tunnel underwent large accelerations over the first two cycles, which then decreased in magnitude as the shaking progressed. The increase in acceleration magnitude over the course of shaking could be due to progressive cyclic softening of the soil, as well as liquefaction, leading to a drop in tunnel-soil system stiffness. This could push the natural frequency of the system down, leading to resonances towards the end of shaking. Alternatively, the initial response of the tunnel could be reduced due to transient effects. If the initial natural frequency of the system is far from the input frequency, the dynamic amplification factor could be less than one, leading to a slow response. Test 3 shows a drift in the average value of acceleration over the course of shaking, due to the large rotation of the tunnel. The final offset of $0.24g$ suggests a final rotation of $sin^{-1}(0.24) = 14^\circ$, which is similar to the value of 15.3° found from PIV tracking (figure 17).

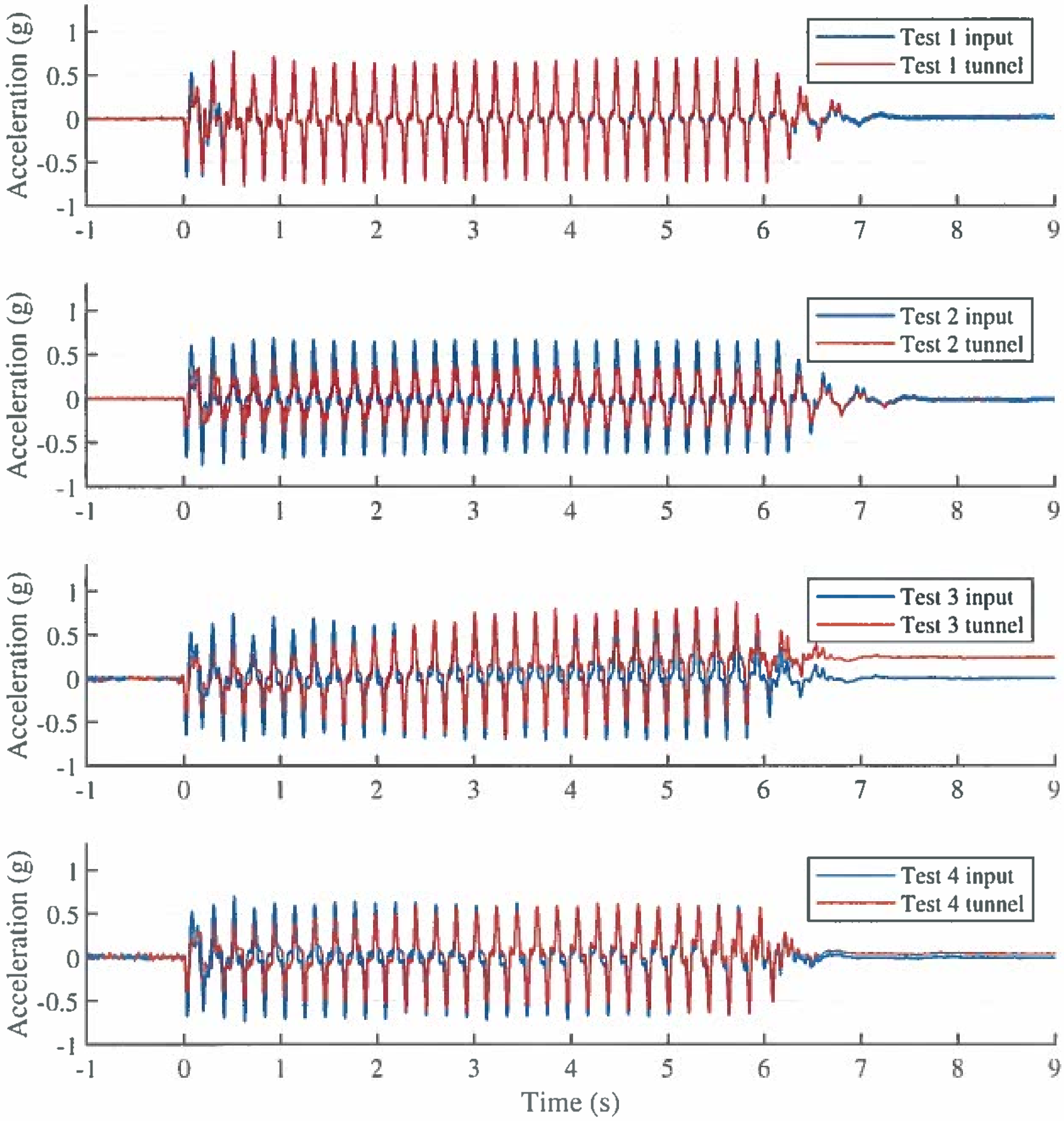

Figure 21: Horizontal accelerations for table input and tunnel crown

7 Soil deformation mechanisms

Video frames displaying each model before and after testing are shown in figures 22a to 25b. Tests 1, 3, and 4 failed by tunnel uplift through the original ground surface, whilst in test 2 the tunnel remained buried.

Figure 22a: Test 1 pre-earthquake

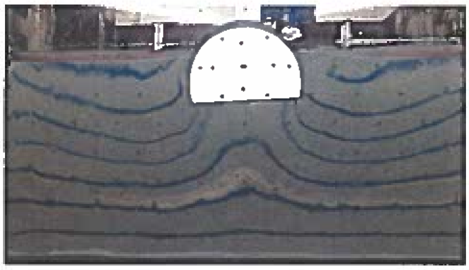

Figure 22b: Test 1 post-earthquake

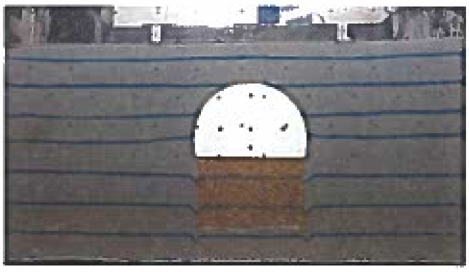

Figure 23a: Test 2 pre-earthquake

Figure 23b: Test 2 post-earthquake

Figure 24a: Test 3 pre-earthquake

Figure 24b: Test 3 post-earthquake

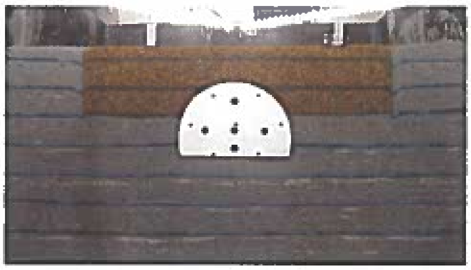

Figure 25a: Test 4 pre-earthquake

Figure 25b: Test 4 post-earthquake

7.1 Net Soil Deformations

Figures 26 to 29 show the cumulative soil deformation mechanisms over the first ten cycles (2 seconds) of shaking, with the corresponding tunnel uplift overlaid. The end of the tenth cycle has been chosen as a common reference point, as it gives sufficient time for the uplift mechanism to develop, whilst the tunnel still remains below the ground surface for all tests, to allow comparison.

The uplift mechanisms formed in tests 1, 3 and 4 are very similar. Deformations of the blue bands in figures 22b, 24b and 25b indicate a large circular uplift mechanism, which is reflected in the PIV outputs. Soil has moved from the crown of the tunnel, down the sides towards the invert, and then up in the tunnel's wake. It is interesting to note the two vortex-like regions at springing level on each side of the tunnel that suggest a highly rotational flow of soil. These may have occurred due to the inability of the liquefied soil to follow a path close to the sharp edges at the base of the tunnel. The majority of the liquefied soil flow to the tunnel invert has occurred by a larger circular flow path, leaving stagnant zones near the springings.

The similarity between the PIV outputs for these tests suggest that granular fill placed above the tunnel is unable to disrupt the soil mechanism that is enabling the uplift. In test 3, the granular fill has been pushed aside by the tunnel as it rises, leading to small trenches of granular fill on each side (figure 24b). Meanwhile in test 4, the granular fill has separated into two large rectangular blocks which have moved down and rotated towards the invert almost intact, indicated by the preservation of the blue bands (figure 25b). This subsidence of the granular fill is due to the buoyant unit weight of the fill being approximately 20% higher than the liquefiable layer. The granular fill follows the flow path of the liquefied soil under its self-weight, and does not disrupt the mechanism, therefore it is not effective at reducing the uplift. The excessive subsidence of the granular fill has also created a large settlement trough, with some liquefied soil flowing back over the outer edges of the subsiding blocks. In reality, this large settlement trough could damage nearby surface structures so this approach would not be appropriate in an urban environment.

In tests 1, 3 and 4, a void opened up across the tunnel invert, suggesting that the pore water was more mobile than the liquefied soil to move in behind the uplifting tunnel. At the end of shaking in test 1, the water in the void was discharged via a sand boil up the right-hand side of the tunnel. This caused the disintegration of the blue bands by the right-hand springing in figure 22b. Meanwhile in tests 3 and 4, as the granular fill blocks sank into the liquefied layer, they moved closer to the invert and hence offered a high hydraulic conductivity path for the water in the void to escape. This resulted in only a thin void remaining after shaking in each case.

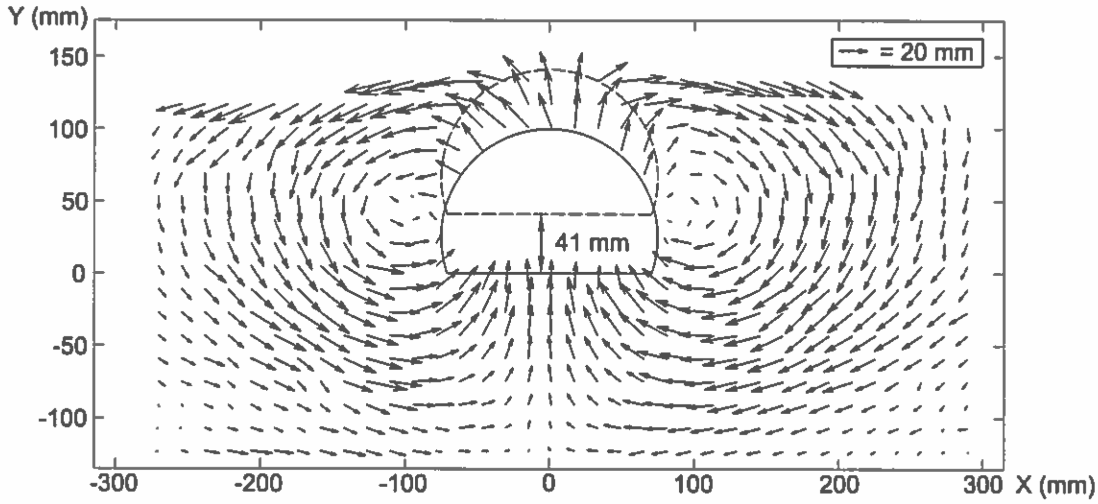

Figure 26: Net soil deformation after 10 cycles of shaking for Test 1

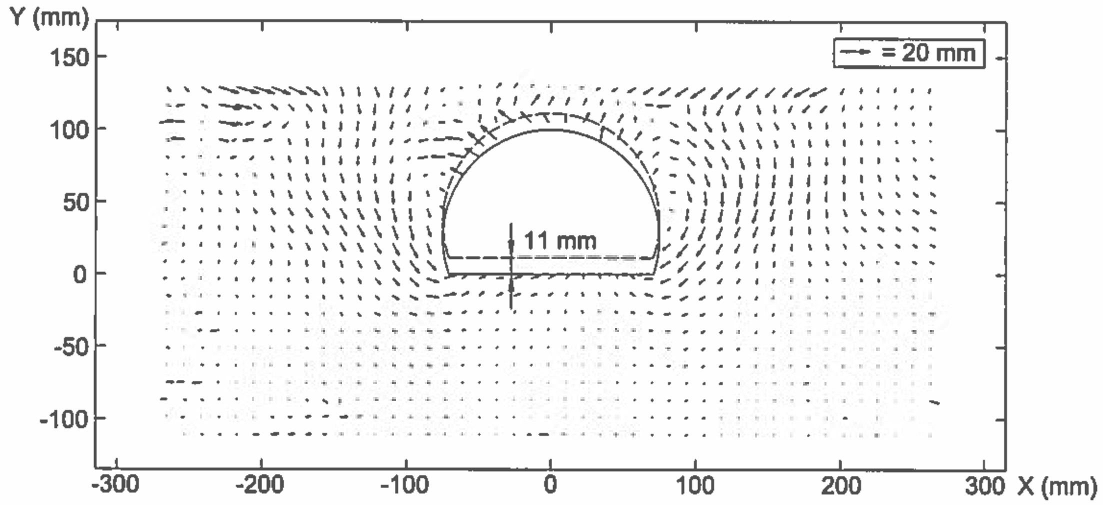

Figure 27: Net soil deformation after 10 cycles of shaking for Test 2

There is a significant difference in the mechanism formed in test 2 compared to the other tests. A large void opened beneath the tunnel within a few cycles of shaking and was maintained throughout the earthquake. The block of compacted granular fill prevented the flow of liquefied soil up behind the tunnel, but its high permeability readily allowed pore water into the tunnel's wake creating the void. Deformation of the blue bands and the PIV output indicate less overall deformation of the soil, which was confined to a much smaller zone around the tunnel. Unlike the large circular flow path seen in the other tests,the soil appears to have moved horizontally into the void beneath the tunnel, forming two triangular wedges seen in figure 23b.

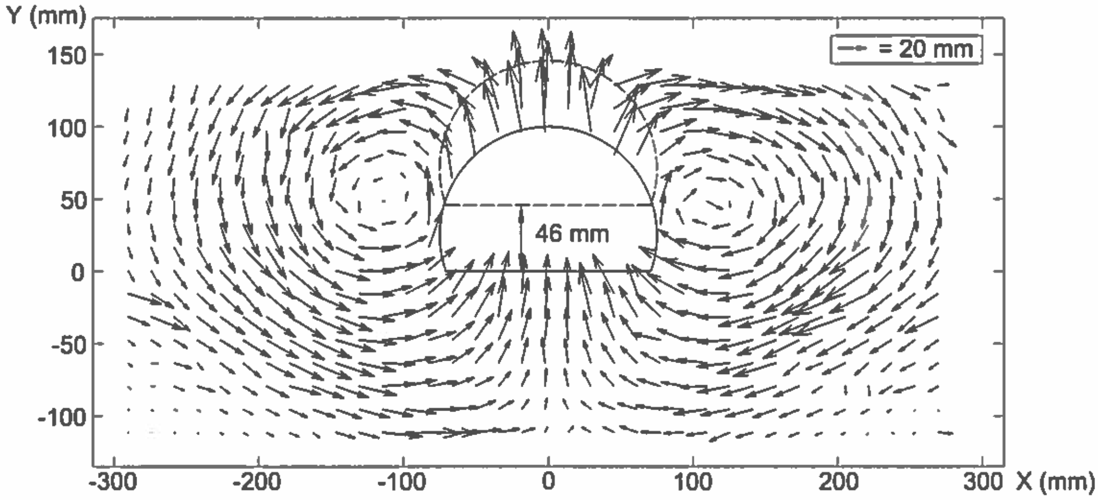

Figure 28: Net soil deformation after 10 cycles of shaking for Test 3

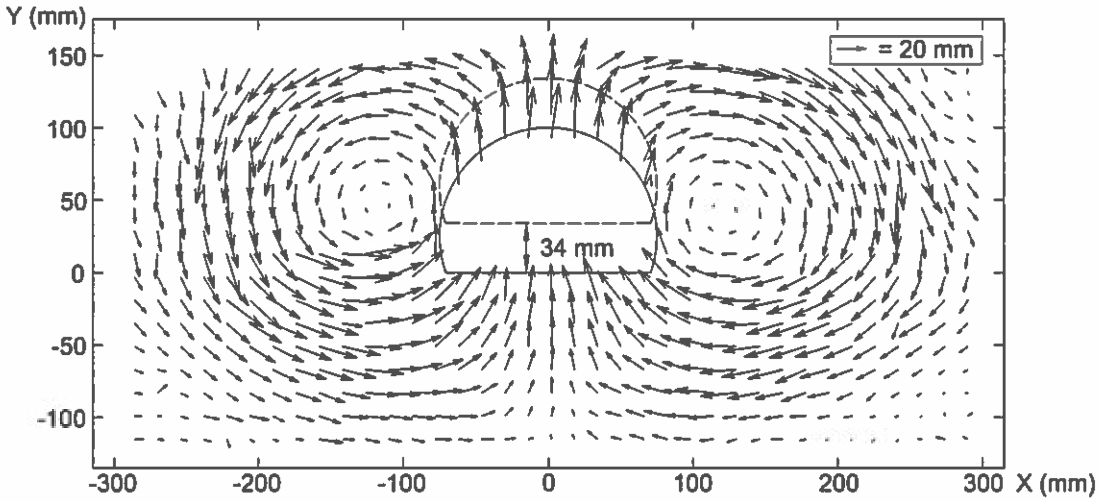

Figure 29: Net soil deformation after 10 cycles of shaking for Test 4

Close inspection of the test video indicates the soil moves in to the void from alternate sides on each half cycle of shaking, which leads to the rocking motion of the tunnel noted in section 4.2. The blue bands and the quiver plot indicate there was little deformation at depths below the tunnel invert. As no PPTs were located in this layer, it is not possible to determine whether this is because this soil did liquefy, but the block of compacted granular fill prevented it from being mobilised in the uplift mechanism, or whether the soil did not liquefy due to its high I_D or drainage into the granular fill.

7.2 Sub-cycle Soil Deformations

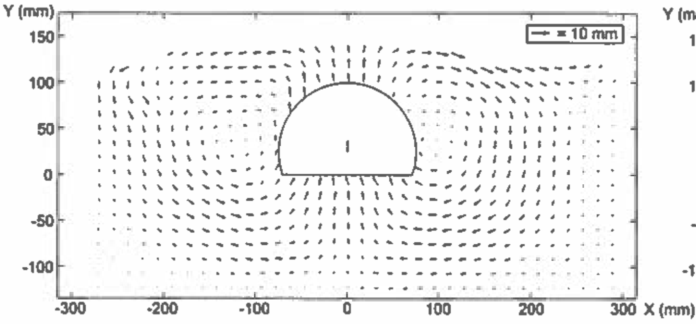

Figure 30a: Test 1 - Full cycle deformation

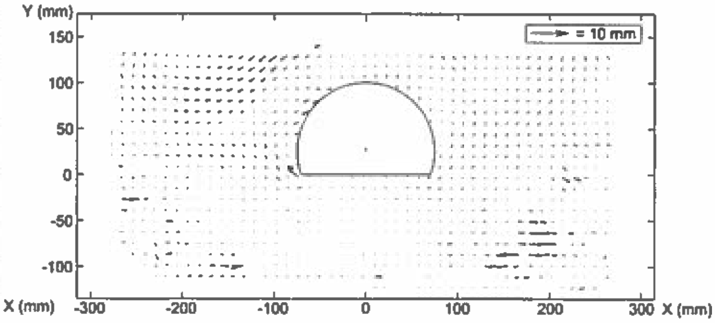

Figure 31a: Test 2 - Full cycle deformation

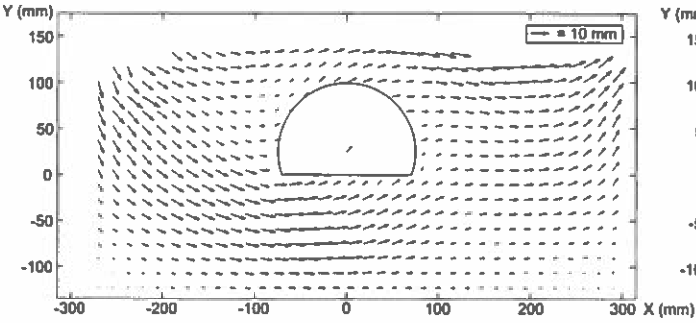

Figure 30b: Test 1 - First half cycle deformation

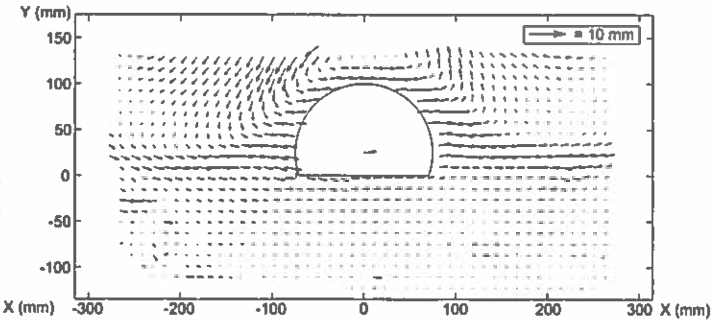

Figure 31b: Test 2 - First half cycle deformation

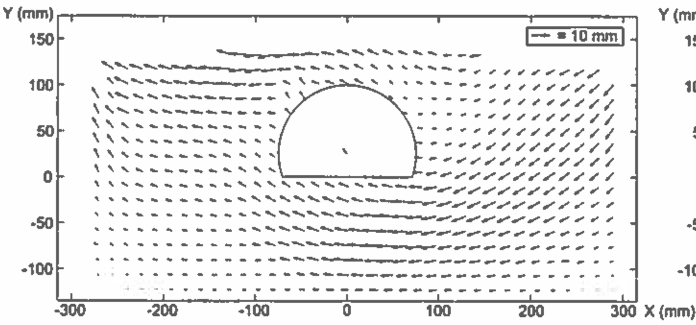

Figure 30c: Test 1 - Second half cycle deformation

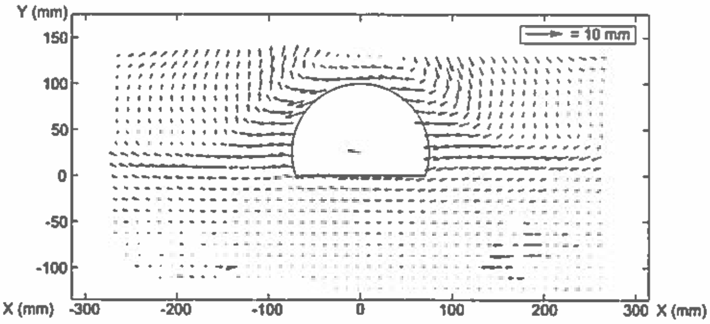

Figure 31c: Test 2 - Second half cycle deformation

Quiver plots showing the soil deformation mechanism over the course of one cycle of shaking along with the mechanisms formed over the two constituent half cycles are shown in figures 30a to 33c. The first half-cycle is defined as when the shaking table moves from the far-right to the far-left of its travel. The second half-cycle is defined as the return from far-left to far-right. The tunnel displacement incurred in each time period considered is plotted in the centre of each tunnel outline.

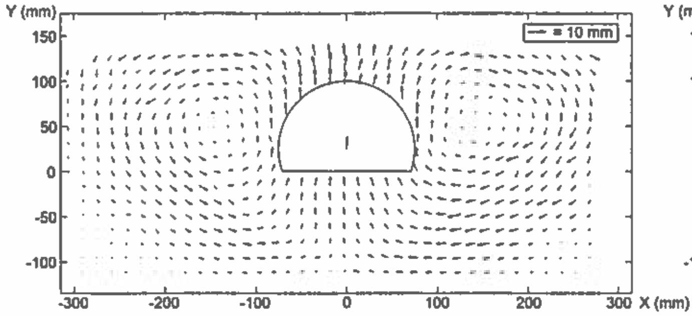

Figure 32a: Test 3 - Full cycle deformation

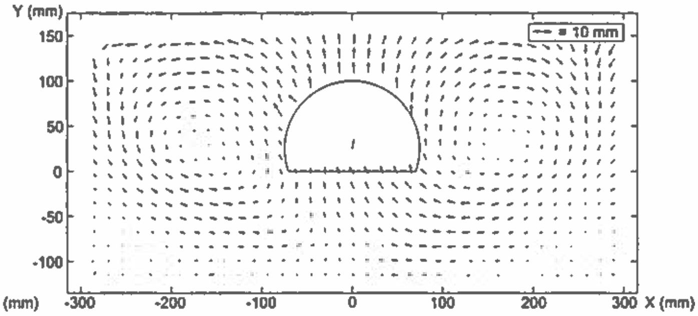

Figure 33a: Test 4 - Full cycle deformation

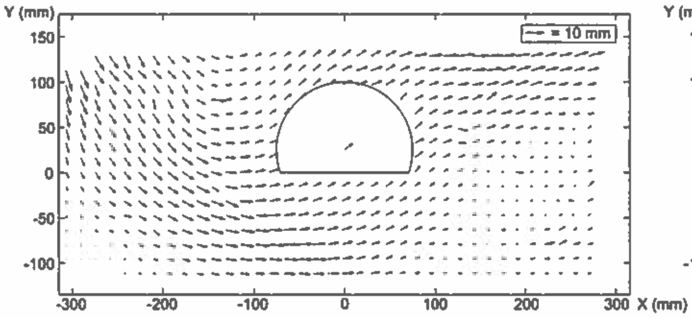

Figure 32b: Test 3 - First half cycle deformation

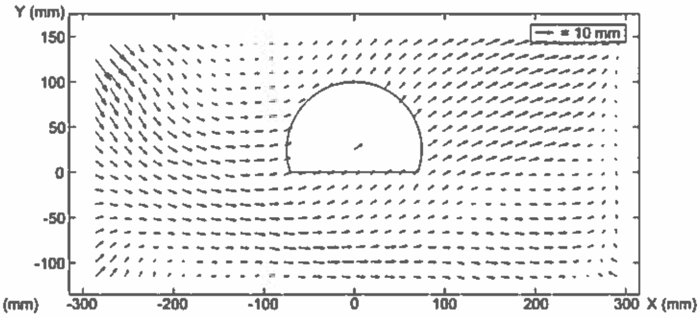

Figure 33b: Test 4 - First half cycle deformation

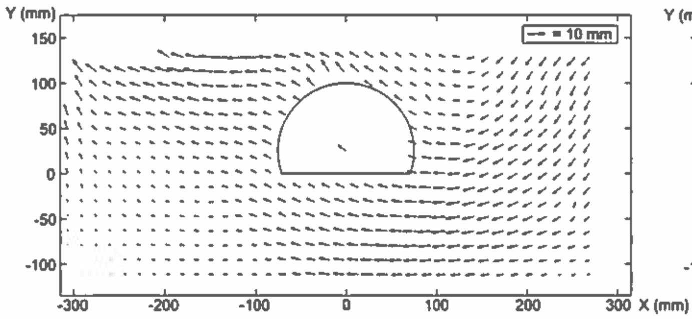

Figure 32c: Test 3 - Second half cycle deformation

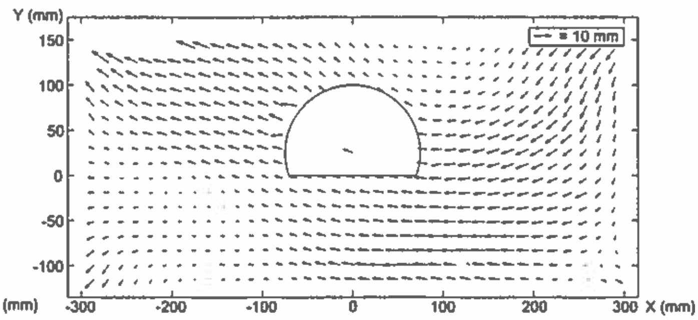

Figure 33c: Test 4 - Second half cycle deformation

Tests 1, 3 and 4 show similar sub-cyclic behaviour, consistent with the similar behaviour seen in the cumulative soil mechanisms in section 7.1. The whole cycle deformations are very similar in shape to the cumulative soil deformations over the first 10 cycles of shaking; however, there appears to be two distinct phases to the uplift mechanism within a cycle. Over the first half cycle, the soil fails on the left-hand side with a large scoop-like mechanism forming around the left edge of the invert. There is then evidence of the soil failing on the right-hand side up an inclined slip plane running from the bottom-centre to top-right of the model. The vector of tunnel displacement runs nearly parallel to this slip plane. During the second half cycle, the soil fails by a large scoop forming around the right edge of the invert, with an inclined slip plane running from bottom-centre to top-left.

These two half-cycle mechanisms are near mirror images of each other, resulting in the near symmetric full-cycle mechanism, which has net vertical displacement and little horizontal displacement of the tunnel. These sub-cyclic mechanisms suggest that, rather than the uplift mechanism being one of a buoyant object in a heavy viscous fluid, in which case a smooth monotonic uplift would be expected, the tunnel is actually uplifting by a ratcheting mechanism. The tunnel slides incrementally up two opposite slip planes on every half-cycle, leading to the significant double-input frequency component in the uplift displacement spectrum observed in section 4.1. The two opposing scoop mechanisms about each edge of the invert over the two half-cycles have lead to the strong rocking response at the input frequency observed in section 4.2.

Test 2 shows very different sub-cyclic behaviour. The upper liquefiable layer appears to split into three distinct zones, separated by slip planes inclined at approximately 45°. A zone around the sides and crown of the tunnel moves mostly horizontally with the tunnel, changing direction on each half-cycle. In the first half-cycle, the soil flow path curves down towards the left-hand edge of the invert, whilst in the second half-cycle, the soil flow path curves down towards the right-hand edge. This has lead to the formation of the two triangular wedges and the strong rocking response observed in the test video and in section 4.2. The upper left and right regions move mostly vertically, alternating between upwards and downwards movement on every half-cycle. There is a marked difference in behaviour above and below invert level. Beneath the invert there is little soil deformation, due to either the block of granular fill preventing mobilisation, or the higher I_D of this soil preventing it being liquefied.

In summary, analysis of the uplift mechanisms mobilised over several cycles and within a cycle have shown that ground improvement beneath the tunnel has greater impact than that above. Compacted granular fill placed beneath the invert and densification of the foundation layer in test 2 has been able to block the formation of the large circular uplift mechanism seen in other tests. By restricting the mobility of the soil, the fourth condition for uplift identified by Smith and Hashash (1999) has not been satisfied and the remediation has been effective at reducing uplift.

8 Comparison With Design Methods

8.1 Factor of Safety Analysis

The Factor of Safety (FoS) was introduced in section 2.2 as the ratio between the resisting and uplifting forces acting on a buried structure. The force components which act on the tunnel as shown in figure 34 in the static and liquefied conditions are defined using the methods of Chian (2012) and detailed in Appendix A.

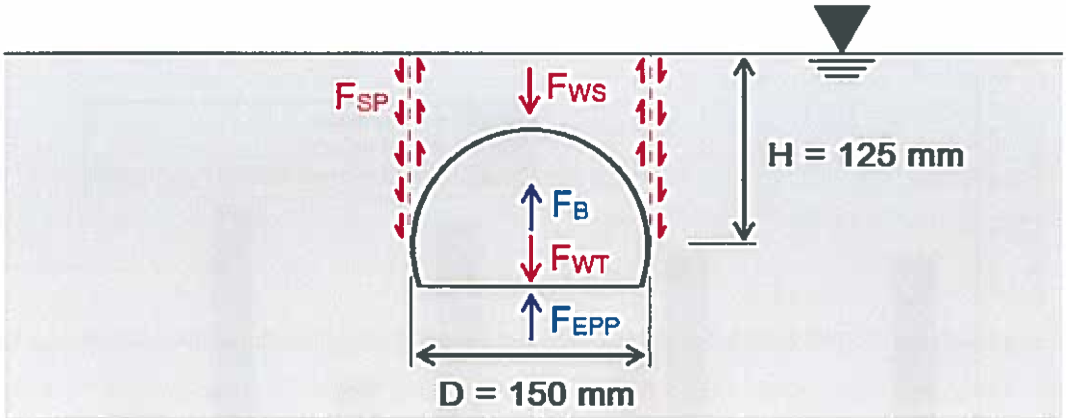

Figure 34: Force components acting on tunnel

This leads to the following definitions of FoS for static and earthquake conditions:

$$FoS_{static} = \frac{F_{resisting}}{F_{uplifting}} = \frac{F_{WT} + F_{WS} + F_{SP}}{F_B} \tag{5}$$

$$FoS_{earthquake} = \frac{F_{resisting}}{F_{uplifting}} = \frac{F_{WT} + F_{WS} + F_{SP,\ reduced}}{F_B + F_{EPP}} \tag{6}$$

The contribution of shear stresses mobilised in the backfill (F_{SP}) have been estimated by assuming a simple mechanism with two vertical shear planes rising from the tunnel springings (consistent with DNV-RP-F110, 2007). In the liquefied condition, this contribution is reduced to $F_{SP,reduced}$ due to EPP reducing horizontal effective stresses acting on the planes. In terms of the liquefaction ratio: $F_{SP,reduced} \sim (1 - r_u)$.

The equations in Appendix A have been used to calculate the FoS for the static and liquefied condition for each test, using information detailed in tables 1 and 2. For the liquefied case, the FoS has been evaluated by considering the EPP generated after one full cycle of shaking, and assuming this is constant across the invert. Additional uplifting force from tension in the potentiometer wire and additional resisting force from friction against the end caps of the tunnel has been neglected as small in this analysis. The resulting FoS are displayed in figure 35. In the static condition, the FoS for each test is greater than one, as expected for no uplift.

For tests 1 and 2, far-field PPT data indicates full liquefaction ($r_u = 1$) is achieved within two cycles of shaking. As liquefaction is a 'top-down' process, it has been assumed full liquefaction occurs on the shear planes and $F_{SP,reduced}$ has been taken as zero. This leads to the FoS falling below one after earthquake initiation, consistent with the observation of uplift occurring. Test 2 retains the highest post-initiation FoS at 0.88, due to having relatively low EPP acting on the invert.

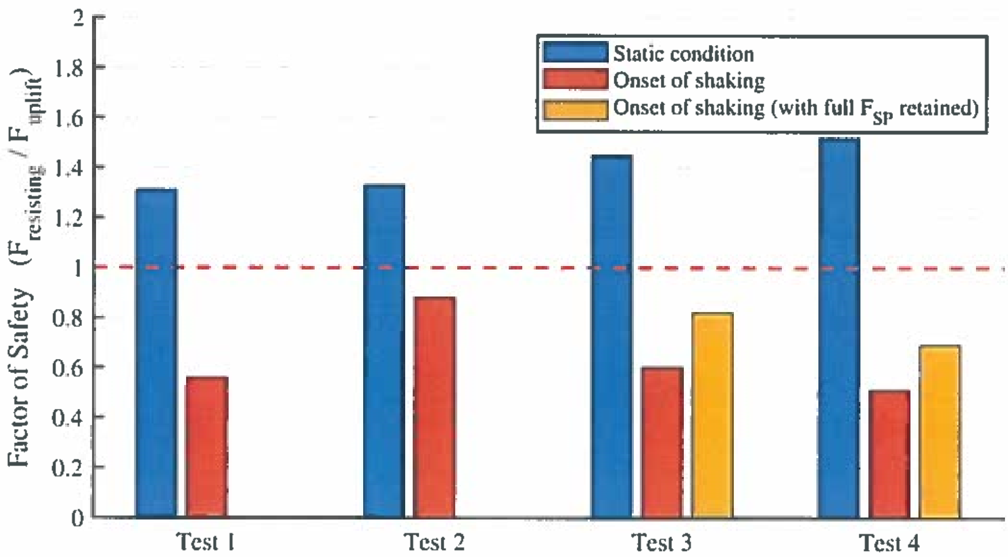

Figure 35: Factors of Safety from experimental results

For tests 3 and 4, the high hydraulic conductivity of the granular fill inclusions will drain away EPP so full liquefaction will not occur. However, liquefaction in the far-field will reduce the lateral confinement on the zone which is drained by the granular fill, therefore the contribution of the shear planes will be reduced. An upper and lower bound on the post-initiation FoS is found by retaining the full original shear strength ($F_{SP,reduced} = F_{SP}$), and by neglecting any shear strength above the tunnel ($F_{SP,reduced} = 0$). Figure 35 shows that even with full F_{SP} retained, the FoS still drops below one due to the rise in EPP. This suggests that, for shallow tunnels at this scale, alleviating EPP acting on the invert is more important than retaining shear strength in the backfill when mitigating uplift risk. However, it must be noted that this observation will be dependent on the burial depth. In the case of full liquefaction, the EPP acting on the invert is equal to the initial effective stress, which scales linearly with depth, hence: $F_{EPP} \sim H$. Meanwhile the contribution of the shear planes is quadratic with depth (see Appendix A), hence: $F_{SP} \sim H^2$. Therefore for deeper tunnels, it could be more important for remediation techniques to target preserving overlying shear strength rather than reducing EPP at the invert.

8.2 Liquefaction Potential Index for Uplifting

The Liquefaction Potential Index for Uplifting (P_L') was introduced in section 2.2 as a method of assessing uplift potential, depending on the resistance of the ground to liquefaction. It is not possible here to evaluate equivalent field-scale values of P_L' due to lack of data and the non-linearity of scaling from 1-g; however, it is possible to compare trends in observations.

The weighting function proposed by Watanbe et al. (2016) indicates that reducing the degree of liquefaction close to the tunnel will have most effect on reducing uplift. This is consistent with the good performance of the remediation in test 2 compared to the reference test. Adding granular fill at the invert will increase F_L in this region and have a large impact on reducing P_L', due to the weighting function, and hence final uplift.

However, the performance of the remediation in tests 3 and 4 compared to the reference test does not seem consistent with the definition of P_L' given above. The presence of the granular fill above the crown should have reduced P_L' and hence led to a lower uplift. This may be because the definition of P_L' proposed by Watanbe et al. (2016) considers only the variation in soil properties with depth. The tests in this investigation have shown that the layout of remediation in two dimensions can influence the uplift mechanism that forms and consequently the final uplift displacement. This relates back to the condition identified by Smith and Hashash (1999) that the liquefied soil must have mobility to flow around the structure to enable uplift. Furthermore, the weighting functions used in the definition of P_L' suggest that the degree of liquefaction of the soil above and below the tunnel are of equal importance, whilst the results in this investigation suggest that liquefaction of the soil beneath the tunnel has a greater influence on uplift than that above.

These discrepancies reinforce the importance of conducting physical model testing, using techniques such as PIV, to gain an insight into the mechanisms behind uplift so that design methods are informed by the physical behaviour of the systems. Further investigation using geotechnical centrifuge modelling may be useful to extend the work of Watanbe et al. (2016) and develop design approaches which consider two-dimensional effects when predicting uplift potential.

9 Conclusion

Uplift failure of buried structures such as tunnels following earthquake-induced liquefaction poses a risk of large economic and human costs. In this project, 1-g shaking table tests have been conducted to investigate potential remediation techniques for this problem via ground improvement using coarse-grained granular fill. Three layouts have been tested with granular fill inclusions above and below the tunnel, along with a reference test.

Ground improvement beneath the tunnel was most successful at reducing uplift, with a final uplift displacement of 25 mm. Ground improvement above the tunnel showed virtually no benefit compared to the reference test, with all achieving uplift displacements of over 65 mm. These observations have been related to the soil deformation mechanisms seen following PIV analysis. When there was no remediation or only ground improvement above the tunnel, the uplift mechanism consisted of large circular soil flow paths on each side of the tunnel, with vortex-like zones near the springings. Meanwhile, with ground improvement beneath the tunnel, the uplift mechanism was limited to small flows of soil down the sides of the tunnel towards the invert. By restricting the flow of liquefied soil around the tunnel, mobilisation of the large circular uplift mechanism was prevented and so the ground improvement beneath the tunnel was successful at limiting uplift.

PIV was also used to analyse the sub-cyclic uplift mechanisms. When there was no remediation or only ground improvement above the tunnel, there were two distinct sub-cyclic soil deformation mechanisms, with the tunnel moving in a block of soil up inclined slip planes, opposite to the direction of input motion, over each half-cycle. With ground improvement beneath the tunnel, the sub-cyclic soil deformations consisted of small flows of liquefied soil beneath the invert, from opposite directions on each half-cycle. These sub-cyclic mechanisms resulted in a double-input frequency cyclic component to the uplift, and rocking of the tunnel at the input frequency as it uplifted.

EPP at the invert and in the far-field was measured. In all cases, the EPP at the invert was lower than in the far-field, due to uplifting of the tunnel reducing the overburden stress (Chian and Madabhushi, 2012; Chain et al., 2014) . In test 2, the EPP at the invert was lower than for all other tests due to the ground improvement beneath the tunnel. This reduced the upwards driving force on the tunnel and so led to a lower uplift. It was observed that oscillations in EPP at the invert occurred at double the input frequency, as expected from the model of liquefaction proposed by Luong and Sidaner (1981), whilst EPP oscillations in the far-field occurred at the input frequency. This could be due to either a monotonic component in shear stress towards the tunnel invert at this point resulting in the characteristic state/phase transformation line being crossed only once every cycle, or inertial forces causing changes in the total stress state of the soil every cycle, as the liquefied soil is accelerated around the circular flow paths.

The uplift behaviour seen was consistent with the expectations from the factor of safety analysis introduced by Chian (2012). For all tests, the calculated *FoS* for the static condition was found to be greater than one, and less than one following the initiation of shaking, hence there was uplift. Further consideration of tests with ground improvement above the tunnel showed that even if the full shear strength of the soil above the tunnel is preserved during shaking, the downwards force produced from assumed vertical shear planes will not be sufficient to maintain a *FoS* greater than one once EPP is generated at the invert. This suggests that alleviating EPP acting on the invert may be more important than preserving shear strength above the tunnel when designing remediation schemes. This effect is likely to be dependent on the burial depth of the tunnel.

The test results have also been compared to the Liquefaction Potential Index for Uplifting (P_L') proposed by Watanbe et al. (2016). This is based on the principle that a *FoS* less than one may be acceptable in design if subsequent uplift is limited such that the structure remains serviceable. Only partial agreement between the test results and the expectations of the P_L' equations were seen. Discrepancies could be due to the importance of blocking the two-dimensional uplift mechanism from forming to limit uplift, seen by comparing test 2 to other tests. This behaviour is not captured in the P_L' method, which considers only one-dimensional variation in soil behaviour. Further investigation using geotechnical centrifuge and/or numerical modelling is needed to gain a better understanding of two-dimensional effects on uplift behaviour, which can then be used to inform design methods.

10 Acknowledgements

I would like to thank all those who have aided me over the course of this project; in particular, I would like to thank my supervisor, Professor Gopal Madabhushi, for his support and guidance. I am also very grateful to the technicians, staff and PhD students of the Schofield Centre for making me feel welcome and offering me a great deal of advice and encouragement.

11 Improvements and Future Work

11.1 Improvements to Methodology

In hindsight, several improvements could have been made to obtain better results. Using sensors more appropriate to 1-g testing rather than centrifuge testing, such as smaller-range PPTs, would have given better data with higher signal-to-noise ratios. Only two working PPTs were available for this investigation; it would have been beneficial to include more PPTs at locations such as the springings and crown, with corresponding far-field measurements, to gain a better understanding of the dynamic soil-structure interaction. Section 4.1 identified that the potentiometer was not able to fully capture the dynamic uplift response of the tunnel. Using only PIV tracking of the tunnel would have been better, as it is able to provide vertical, horizontal and rotational displacements, and would have removed the spurious tensile force applied to the tunnel by the potentiometer wire.

Improvements could also have been made during model preparation. Manually pouring sand from the suspended hopper resulted in some variability in the relative density of the liquefiable layer. Using the automatic sand pourer as used for preparing centrifuge models would have given more consistent density. Saturation of the models under atmospheric conditions was not able to achieve very high levels of saturation ratio. This was a problem in tests 3 and 4 as the release of air bubbles during shaking reduced the degree of liquefaction, affected PPT measurements, and smeared the deformation mechanisms seen against the Perspex window. Using the centrifuge model procedure of pumping the model with carbon dioxide then saturating under vacuum would have led to more complete saturation.

11.2 Future Work

The outcomes of this investigation suggest several avenues for future work. Repeating the tests in a geotechnical centrifuge would provide scalable results that could give a better insight into the behaviour of the tunnel with different remediation layouts. In addition, the results of this investigation indicate that ground improvement by granular fill replacement (and densification) is more effective when placed beneath the tunnel rather than above the tunnel. Future work could investigate if this trend is reflected for other methods of ground improvement such as grouting, drainage columns, and densification alone. It is important to note that implementing the remediation layouts proposed here would be very expensive in reality, as extensive excavation and fill replacement would be required along the tunnel. Future work could aim to optimise the geometry of the granular fill inclusions, targeting areas beneath the tunnel, to minimise the amount of material used.

12 References

Adalier, K., Abdoun, T., Dobry, R., Phillips, R., Yang, D. and Nabsgaard, E. (2003) - "Centrifuge Modelling for Seismic Retrofit Design of an Immersed Tube Tunnel", International Journal of Physical Modelling in Geotechnics, 3(2):23-25

Bradley, S. (2017) "Modelling Tunnel Response during Earthquake-Induced Liquefaction", Unpublished M.Eng project, University of Cambridge

Castiglia, M., Morgante, S., Napolitano, A., and De Magistris, F.S. (2017) - "Mitigation measures for the stability of pipelines in liquefiable soils", Journal of Pipeline Engineering, 16:115-139

Chang, D., Travasarou, T., and Chacko, J.M. (2008) - "Numerical evaluation of liquefaction-induced uplift for an immersed tunnel", Proceedings of 14th World Conference on Earthquake Engineering, Beijing

Chian, S.C. (2012) - "Floatation of Underground Structures in Liquefiable Soils", Unpublished PhD thesis, University of Cambridge

Chain, S.C. and Madabhushi, S.P.G. (2012) - "Excess Pore Pressure Around Underground Structures Following Earthquake Induced Liquefaction", International Journal of Geotechnical Earthquake Engineering, 3(2):25-41

Chian, S.C. and Madabhushi, S.P.G. (2013) - "Remediation against floatation of underground structures", Proceedings of the Institution of Civil Engineers - Ground Improvement, 166(3):155-167

Chian, S.C., Tokimatsu, K. and Madabhushi, S.P.G. (2014) - "Soil Liquefaction-Induced Uplift of Underground Structures: Physical and Numerical Modeling", ASCE Journal of Geotechnical and Geoenvironmental Engineering, 140(10), 04014057

Chou, J.C., Kutter, B.L., and Travasarou, T. (2010) - "Numerical Analyses of Centrifuge Models of the Bart Transbay Tube", Proceedings of Fifth International Conference on Recent Advances in Geotechnical Earthquake Engineering and Soil Dynamics, San Diego

Chou, J.C., Kutter, B.L., Travasarou, T., and Chacko, J. M. (2011) - "Centrifuge modelling of seismically induced uplift for the BART Transbay Tube", Journal of Geotechnical and Geoenvironmental Engineering, 137(8):754-765

Dhoru, D. (2018) - "Tunnel Floatation in Liquified Soils", Unpublished M.Eng project, University of Cambridge

DNV-RP-F110 (2007) - "Global buckling of submarine pipelines", Recommended Practice, Det Norske Veritas, Nøvik

Hazen, A. (1911) - "Discussion: dams on sand foundations", Transactions, American Society of Civil Engineers, 73:199-203.

Heron, C.M., Haigh, S.K., and Madabhushi, S.P.G. (2014) - "Isolating shallow foundations from seismic loading", Proceedings of the 8th International Conference on Physical Modelling in Geotechnics, Perth, pp.621-627

Hughes, F.E., and Madabhushi, S.P.G. (2018) - "The importance of vertical acceleration in liquefied soils", Proceedings of the 9th International Conference on Physical Modelling in Geotechnics, London, pp.967-973

Ishihara, K., Tatsuoka, F. and Yasuda, S. (1975) - "Undrained deformation and liquefaction of sand under cyclic stresses", Soils and Foundations, 15(1):29-44

Iwasaki, T., Tokida, K., Tatsuko, F., and Yasuda, S. (1978) - "A practical method for assessing soil liquefaction potential based on case studies at various sites in Japan", Proceedings of 2nd International Conference on Microzonation, San Francisco, pp.885-896

Iwasaki, T., Arakawa, T., and Tokida, K. (1982) - "Simplified procedures for assessing soil liquefaction during earthquakes", Proceedings of the Conference on Soil Dynamics and Earthquake Engineering, Southampton, pp.925-939

Jenkins, M. (2015) - "Characterisation of Floatation of Rectangular Tunnels Following Earthquake Induced Liquefaction", Unpublished M.Eng project, University of Cambridge

Kutter, B.L., Chou, J.C. and Travasarou, T. (2008) - "Centrifuge testing of the seismic performance of a submerged cut-and-cover tunnel in liquefiable soil", Geotechnical Special Publications, No. 181, Proceedings of Geotechnical Earthquake Engineering and Soil Dynamics IV Congress, Sacramento

Luong, M.P. and Sidaner, J.F. (1981) - "Undrained behavior of cohesionless soils under cyclic and transient loading", Proceedings of the International Conference on Recent Advances in Geotechnical Earthquake Engineering and Soil Dynamics, St. Louis, pp.215-220.

Madabhushi, S.P.G. (2007) - "Ground improvement methods for liquefaction remediation", Ground Improvement, 11(4):195-206

Madabhushi, S.P.G. (2019) - "Excess pore pressures, Liquefaction & Liquefaction Resistant Design", [Lecture] Cambridge University Engineering Department, 5th March

Martin, G.R., Finn, W.D.L., and Seed, H.B. (1975) - "Fundementals of Liquefaction under Cyclic Loading", Journal of Geotechnical Engineering Division, ASCE, 101:423-438

MathWorks (2019) - MATLAB 'filtfilt' function documentation, https://uk.mathworks.com/help/signal/ref/filtfilt.html, Accessed: 07/05/2019

Mitrani, H. (2006) - "Liquefaction remediation techniques for existing buildings", Unpublished PhD thesis, University of Cambridge

Otsubo, M., Towhata, I., Hayashida, T., Shimura, M., Uchimura, T., Liu, B., Taeseri, D., Cauvin, B., and Rattez, H. (2016a) - "Shaking table tests on mitigation of liquefaction vulnerability for existing embedded lifelines", Soils and Foundations, 56(3):348-364

Otsubo, M., Towhata, I., Hayashida, T., Liu, B., and Goto, S. (2016b) - "Shaking table tests on liquefaction mitigation of embedded lifelines by backfilling with recycled materials", Soils and Foundations, 56(3):365-378

Pease, J.W. and O'Rourke, T.D. (1997) - "Seismic response of liquefaction sites", Journal of Geotechnical and Geoenvironmental Engineering, ASCE, 123(1):37-45.

Room, E. (2014) - "Visualisation of floatation of tunnels following earthquake induced liquefaction", Unpublished M.Eng project, University of Cambridge

Rouhanifar, S., and Ibraim, E. (2015) - "Laboratory investigation on the mechanics of soft-rigid soil mixtures", Proceedings of the 6th International Symposium on Deformation Characteristics of Geomaterials, Buenos Aires, pp.1073-1080

Schmidt, B. and Hashash, Y.M.A. (1999) - "Preventing tunnel flotation due to liquefaction", Proceedings of the 2nd International Conference on Earthquake Geotechnical Engineering, Lisboa, pp.509-512

Seed, H. B. and Idriss, I. M. (1982) - "Ground Motions and Soil Liquefaction During Earthquakes", Earthquake Engineering Research Institute

Stanier, S.A., Blaber, J., Take, W.A. and White, D.J. (2015) - "Improved image-based deformation measurement for geotechnical applications", Canadian Geotechnical Journal, 53:727-739

Structural Engineers Association of Washington (2011) - "2011 Great East Japan (Tohoku) Earthquake & Tsunami Reconnaissance Report", https://www.seaw.org/s/seaw-2011japaneqreport.pdf, Accessed: 19/11/2018

Taylor, P.R., Ibrahim, H.H., and Yang, D. (2005) - "Seismic retrofit of George Massey Tunnel", Earthquake Engineering and Structural Dynamics, 34:519-542

Tokimatsu, K., Suzuki, H., Katsumata, K. and Tamura, S. (2013) - "Geotechnical Problems in the 2011 Tohoku Pacific Earthquakes", Proceedings of the 7th International Conference on Case Histories in Geotechnical Engineering, Chicago

Watanabe, K., Sawada, R., and Koseki, J. (2016) - "Uplift mechanism of open-cut tunnel in liquefied ground and simplified method to evaluate the stability against uplifting", Soils and Foundations, 56(3):412-426

White, D.J. and Take, W.A. (2002) - "GeoPIV: Particle Image Velocimetry (PIV) software for use in geotechnical testing", Technical report 322, University of Cambridge

Wright, T. (2016) - "Floatation of Rectangular Tunnels in Liquidable Soils", Unpublished M.Eng project, University of Cambridge

Yanamoto, T., Tateishi, A. and Tsuchiya, M. (2014) - "Seismic design for immersed tube tunnel and its connection with TBM tunnel in Maramaray project", Proceedings of the Second European Conference on Earthquake Engineering and Seismology, Istanbul

13 Appendices

Appendix A - Force Components on Tunnel

The following is defined for the free body diagram described by the shear planes and tunnel base in figure 34. The buoyancy of the tunnel is given by Archimedes principle:

$$F_B = V_{tunnel} \cdot \gamma_w \tag{7}$$

This definition with the unit weight of water is used for both the static and liquefied case. Additional buoyant effects due to liquefaction turning the soil into a heavy fluid are encapsulated in F_{EPP}.
In the liquefied case, the upwards force due to EPP can be estimated by assuming the EPP measured by the invert PPT is constant over the invert:

$$F_{EPP} = \int_A u_{EPP} \cdot dA = u_{EPP} \cdot A_{invert} \tag{8}$$

The self-weight of the tunnel is given by:

$$F_{WT} = M_{tunnel} \cdot g \tag{9}$$

where M_{tunnel} is the mass measured after testing, to allow for water ingress following saturation.
The effective weight of the overburden soil acting on the tunnel is given by:

$$F_{WS} = \left(H \cdot D - \frac{1}{2} \cdot \frac{\pi D^2}{4} \right) \cdot L \cdot \gamma' \tag{10}$$

This definition using the buoyant weight, along with the tunnel buoyancy term (F_B) accounts for hydrostatic pore pressures acting on the base of the free body of the tunnel and overburden soil.

The contribution of shear stresses mobilised in the overburden soil are estimated by assuming a simple mechanism with two vertical shear planes rising from the tunnel springings. By considering the stresses on these planes in the static condition:

$$F_{SP} = 2 \int_0^H \tau \cdot L \cdot dz = 2 \int_0^H \sigma_h' \cdot tan(\phi') \cdot L \cdot dz = 2 \int_0^H K_o \cdot \gamma' \cdot z \cdot tan(\phi') \cdot L \cdot dz$$

$$\Rightarrow F_{SP} = K_o \cdot \gamma' \cdot tan(\phi') \cdot H^2 \cdot L \tag{11}$$

where $K_o = (1 - sin(\phi'))$. This is consistent with the results provided by the code of practice for Global Buckling of Submarine Pipelines (DNV-RP-F110, 2007). In the liquefied condition, horizontal effective stresses on the shear planes are reduced due to EPP, expressible as:

$$\sigma_h' = K_o \cdot \sigma_v' = K_o(\sigma_{vo}' - u_{EPP}) = K_o \cdot \sigma_{vo}'(1 - r_u)$$

where r_u is the liquefaction ratio defined in section 2.1. Hence the force component from the shear planes reduces to:

$$F_{SP,\ reduced} = K_o \cdot \gamma' \cdot tan(\phi') \cdot L \int_0^H z(1 - r_u)dz \tag{12}$$

Appendix B - Retrospective Risk Assessment

A comprehensive risk assessment was conducted before any experimental work began. The risk assessment was based on experience reported from past MEng projects and covered all hazards encountered. Specific hazards and control measures include:

- *Moving parts / entanglement* - The shaking table motor/actuator was located behind safety guards. All people and other equipment were kept clear of shaking table when in operation
- *Electric shock* - All electrical equipment and wiring was checked for its condition before use. Only waterproofed equipment came into contact with water.
- *Dust* - Mixing of sand produced a significant amount of dust. Mixing of sand was conducted outside where possible, wearing a ventilated mask. Any indoor handling of sand was conducted in the model preparation room under the extractor fan.
- *Slip, trips, and falls* - The project work area was kept clean and tidy. All cables/wires were routed away from walkways and covered with cable mats where appropriate. The work area was swept clean as necessary.
- *Burns* - Only LED lights were used. Thick gloves were used when moving items in/out of ovens. Drying sand on the hotplate was conducted under the extractor fans and with warning signs visible.
- *Manual handling* - Care was taken to use proper form when lifting heavy items and assistance was obtained when necessary.
- *Use of chemicals* (Blue layout ink, Plastidip spray, Gloss Varnish) - PPE including a ventilated mask, rubber gloves and a lab coat was worn when handling chemicals. Volatile chemicals (especially blue layout ink) were used outside or under extractor fans.